# Complex dynamics and multistability of driven diatomic molecules revealed by numerical modelling of shifted molecular potentials

O. T. Kolebaje,[1,*] U. E. Vincent,[2,3,†] and P. V. E. McClintock[3]

[1] *Department of Physics, Adeyemi Federal University of Education, Ondo 350106, Nigeria*
[2] *Department of Physical Sciences, Redeemer's University, Ede 232101, Nigeria*
[3] *Department of Physics, Lancaster University, Lancaster LA1 4YB, United Kingdom*

(Dated: September 20, 2025)

We have explored the nonlinear dynamics of six common, driven, diatomic molecules using a shifted Tietz-Wei (sTW) model of their molecular potential functions. We focused on the variations in their resonances, bifurcations and multistability with changes in the spectroscopic and driving force parameters, namely, the dissociation energy ($V_0$), the potential function optimization parameters ($b_h$ and $c_h$), driving frequency ($\omega$), and amplitude ($F_0$). We used the method of multiple time-scales to obtain frequency response curves for the primary and secondary superharmonic resonances. The primary resonances were larger for $I_2$ and $Cl_2$ than for CO or $O_2$. Variations in $F_0$, $b_h$, and $c_h$ had profound impacts on the primary resonance features, with higher $F_0$ and lower $V_0$ enhancing the response amplitude. Evidence for hysteresis in the frequency-response – a signature of multistability – is demonstrated. Superharmonic resonances are marked by increased amplitudes and significant hysteresis, especially for $I_2$ and $Cl_2$, driven by large $F_0$ at low $V_0$. Bifurcation diagrams, maximal Lyapunov exponents, and Poincaré maps were used to unravel the transitions between periodic and chaotic states. Period-doubling bifurcations, sudden chaos, and an abundance of crisis events, viz boundary, interior, and attractor-merging crises, were identified as the routes to a range of different chaotic states. Symmetry-breaking, attractor-bubbling, and multistability were all found and are reported. Coexisting attractors and their basins of attraction showed striped, fractal, and Wada-like basin structures. The results highlight the complex dynamics stemming from the interaction between spectroscopic properties and external excitations of the sTW oscillator in diatomic molecules. They carry significant implications for experimental applications.

## I. INTRODUCTION

Driven nonlinear systems are known to exhibit a wide range of complex and intriguing phenomena [1] such as bifurcations [2–7], chaos [2–4], antimonotonicity [8, 9], bursting and mixed-mode oscillations [10–13], nonlinear resonance [14–17], synchronization [4, 18–21], and multistability [22–27]. Chaotic dynamics and the multistability of attractors have been closely studied in a wide range of nonlinear systems and our knowledge of their occurrence, together with applications, have been greatly enriched [26, 27]. Yet the emergence of chaotic behaviors in dynamical systems is often preceded by diverse bifurcation transition mechanisms, such as period-doubling and crises, among other events [3], which remain less explored. Multistability and its variants, namely, extreme multistability [28–30], and megastability [31–33] are characterized by the coexistence of two or more attractors, either periodic or chaotic or a combination of them, for fixed parameter values [26–33]. For extreme multistability, it is generally known that an infinite number of attractors can coexist. Thus, the system can exhibit an uncountable number of stable states with each corresponding to a different attractor [28–30]. In contrast, megastability involves a countable number of coexisting attractors - meaning that the system can switch between a large, but countable number of states [31–33]. A special variant of multistability was very recently announced [34]. It was referred to as *Matryoshka multistability*. In this case, an infinite number of exactly self-similar attractors which are embedded inside each other coexist in a system [34]. These multistable scenarios give rise to highly complex and unpredictable behaviors.

Starting from the early exploration of multistability by Hennri Poincaré in the 19th century, from the viewpoint of homoclinic behavior in dynamical systems, to very recent comprehensive reports of its occurrences in diverse systems [26, 27, 35], the multistability of attractors has become fundamental to a wide range of investigations of both physical and biological systems [27]. This is on account of e.g. their roles in the attainment of stable synchronous states of interacting oscillators [36], in the understanding of memory and cognitive processes in neurons [37, 38], in the design of memory electronic circuits capable of switching between multiple stable behaviors [39, 40], in cryptography and secure communications [29, 41–43], in the design of micro- and nanosystems [44], and in improving the efficiency of energy harvesting [45, 46] as well as in thermochemical reactors [47]. There are many other examples.

Motivated in part by these useful applications of multistability, in part by the inherent interest of this widespread phenomenon, and in part by the excellent pedagogical review by Pisarchik and Hramov [27], extensive efforts have been made to explore the manifestations and features of multistability. These have in-

* olusolakolebaje2008@gmail.com
† Corresponding author:u.vincent@lancaster.ac.uk

cluded, for example, a range of driven nonlinear oscillators [30, 48–51], chemical system [52, 53], plasma models [54–56], non-smooth nonlinear systems [57, 58], quantum systems [59], mammalian cells [60], mechanical systems [45, 46] and optomechanical devices [61–65]. Despite these numerous studies, multistability in the shifted sTW oscillator proposed by Falaye *et al.* [66] has not yet, to our knowledge, been investigated.

The sTW oscillator is a Morse-type molecular potential used for describing atomic interactions in diatomic molecules. It was introduced to model molecular dynamics at moderate and high rotational and vibrational quantum numbers, and represents a successful attempt by Falaye *et al.* [66] to find an appropriate potential function for studying the vibrational, dynamical and thermodynamic properties of diatomic molecules. Diatomic molecules are integral to numerous natural and industrial processes and applications, including atmospheric chemistry [67], combustion [68], laser spectroscopy [69–71], astrophysics [72, 73], material science [74], and nuclear reactors [75], underscoring their scientific importance. The sTW potential function offer several advantages over the traditional Morse potential. These include greater flexibility in fitting experimental data due to additional adjustable parameters, improved accuracy in describing molecular interactions at high vibrational and rotational quantum states, and better representation of the dissociation energy and anharmonic effects [76, 77]. The sTW potential function has been investigated in great detail and employed to obtain the bound and scattering states, rotation–vibration spectra, and molar entropy of diatomic molecules [78–85]. None of these reports explored the dynamics of the sTW oscillator within the framework of dissipative-driven nonlinear dynamical systems for interatomic potentials [86–89]. As a first step towards addressing this gap, we recently investigated the classical motion of a dual-frequency driven oscillator in an sTW potential function [77]. While exploring the vibrational dynamics, we found discontinuous resonance jumps, of the kind often associated with dynamical hysteresis – a signature of the existence of different coexisting states for a single set of parameter values, such that the dynamics is irreversible when a parameter is varied forwards and back again. Motivated by these observations, we explore in this present paper, the nonlinear dynamics of the driven sTW oscillator, paying particular attention to its resonances, hysteresis, bifurcations and multistability, and the roles played by the sTW potential function parameters, namely, $V_0$, $c_h$, and $b_h$l on their occurrence. Because the sTW model provides such an excellent description of diatomic molecules, it is to be expected that phenomena that we observe and report in the model will also be manifested in the actual physical molecules. They can therefore be sought experimentally by experts working in the area.

The rest of the paper is organized as follows: Section II introduces the model equation of motion for the shifted sTW oscillator. Section III provides a theoretical investigation of its primary and secondary resonance responses under external forcing. Section IV presents the observed bifurcation structures, highlighting the system's complex dynamical behaviors, and including the appearance of multistability. Finally, Section V summarizes the key findings and offers concluding remarks.

## II. THE MODEL

We investigate the classical dissipative and driven sTW oscillator described by the equation of motion [77]:

$$\ddot{x} + \delta\dot{x} + \frac{dV(x)}{dx} = f\cos\omega t \tag{1}$$

where $x$ is the inter-nuclear distance, $\delta$ is the damping coefficient, and $f$ is the amplitude of the external forcing at angular frequency $\omega$. $V(x)$ is the sTW potential defined by [66, 79]:

$$V(x) = V_0\left(\frac{Ae^{-b_h(x-r_e)} - Be^{-2b_h(x-r_e)}}{(1-c_he^{-b_h(x-r_e)})^2}\right), \tag{2}$$

where $A = 2(c_h - 1)$, $B = (c_h^2 - 1)$, $b_h = \gamma(1 - c_h)$, $V_0$ is the potential well depth or dissociation constant, $r_e$ is the molecular bond length at the equilibrium radius, $c_h$ is the optimization parameter obtained *ab initio* or Rydberg–Klein–Rees (RKR) intramolecular potential, and $\gamma$ is the Morse constant [66, 85], defined as $\gamma = \omega_e\sqrt{2\pi^2\frac{c^2\mu}{V_0}}$, with $\mu$ and $c$ being the reduced mass and the speed of light, respectively. In the limit of the optimization parameter approaching zero, i.e. $c_h \to 0$, the sTW potential reduces to the popular Morse potential [66, 85, 90]. Except where otherwise stated, we fix the parameters at $\delta = 0.8$, $f = 4.0$, $\omega = 3.0$, $V_0 = 1$, $c_h = 0.25$, and $b_h = 1.0$, $r_e = 0$. Table I summarizes the key molecular parameters of the sTW potential functions for the six diatomic molecules herein examined, including the reduced mass ($\mu$), equilibrium bond length ($r_e$), dissociation energy ($V_0$), and potential parameters ($b_h$ and $c_h$).

In order to analyze Eq. (1), it is convenient to express $V(x)$ in terms of a new variable, $z$, such that,

$$z = e^{-b_h(x-r_e)}. \tag{3}$$

In terms of $z$, Eq. (1) can be written as;

$$V(x) = V_0\left(\frac{Az - Bz^2}{(1-c_hz)^2}\right), \tag{4}$$

with $\frac{dV(x)}{dx}$ in terms of $z$, given as,

$$\frac{dV}{dx} = -V_0b_hz\left(\frac{(A(1+c_hz) - 2Bz)}{(1-c_hz)^3}\right). \tag{5}$$

TABLE I. Spectroscopic parameter values for 6 diatomic molecules modeled by the shifted Tietz-Wei molecular potential [77, 91–94].

| Molecule | $\mu$ (u) | $r_e$ (Å) | $V_0$ (eV) | $b_h$ (Å$^{-1}$) | $c_h$ |
|---|---|---|---|---|---|
| CO | 6.8607 | 1.1283 | 10.845 | 2.2048 | 0.1499 |
| $O_2$ | 7.9975 | 1.208 | 5.1567 | 2.5910 | 0.0273 |
| $I_2$ | 63.4522 | 2.662 | 1.5818 | 2.1234 | 0.1390 |
| $H_2$ | 0.5039 | 0.7416 | 4.7446 | 1.6189 | 0.1701 |
| $Cl_2$ | 17.6083 | 1.987 | 2.5139 | 2.2035 | 0.0970 |
| HF | 9.5014 | 0.917 | 6.120 | 1.9421 | 0.1278 |

## III. RESONANCE ANALYSIS OF THE SHIFTED TIETZ-WEI OSCILLATOR

We now present a theoretical analysis of the primary and secondary resonance responses of the sTW oscillator (1) under forced external excitation. Let $y = x - r_e$, $\dot{y} = \dot{x}$, $\ddot{y} = \ddot{x}$. Then the oscillator becomes

$$\ddot{y} + d\dot{y} - V_0 b_h e^{-b_h y}\left[\frac{A(1+c_h e^{-b_h y}) - 2Be^{-b_h y}}{(1-c_h e^{-b_h y})^3}\right] = f\cos\omega t. \quad (6)$$

To facilitate the analysis, we Taylor-expand the potential function, obtaining

$$- V_0 b_h e^{-b_h y}\left[\frac{A(1+c_h e^{-b_h y}) - 2Be^{-b_h y}}{(1-c_h e^{-b_h y})^3}\right] = \beta_0 + \beta_1 y + \beta_2 y^2 + \beta_3 y^3 + \ldots, \quad (7)$$

where

$$\beta_0 = -V_0 b_h\left[\frac{A(1+c_h) - 2B}{(1-c_h)^3}\right],$$

$$\beta_1 = V_0 b_h^2\left[\frac{A - 2B(2+c_h) + Ac_h(4+c_h)}{(1-c_h)^4}\right] = \omega_0^2,$$

$$\beta_2 = -\frac{V_0 b_h^3}{2(1-c_h)^5}\left[A(1+c_h)(1+c_h(10+c_h)) - 2B(4+c_h(7+c_h))\right], \quad (8)$$

$$\beta_3 = \frac{V_0 b_h^4}{6(1-c_h)^6}\left[A - 2B(8+c_h(33+c_h(18+c_h))) + Ac_h(26+c_h(66+c_h(26+c_h)))\right]. \quad (9)$$

This reduces the oscillator equation to:

$$\ddot{y} + d\dot{y} + \beta_0 + \omega_0^2 y + \beta_2 y^2 + \beta_3 y^3 = f\cos\omega t. \quad (10)$$

### A. Primary Resonance

In the case of the primary resonant state, the amplitude of the external excitation $f$ is small and proportional to a perturbation parameter $\epsilon$, such that $f = \epsilon F_0$. We also set $d = \epsilon d$, $\beta_2 = \epsilon\beta_2$, and $\beta_3 = \epsilon\beta_3$. The relationship between the external excitation frequency $\omega$ and the natural frequency $\omega_0$ is expressed as $\omega = \omega_0 + \epsilon\sigma$, where $\sigma$ is the detuning parameter. Consequently, the perturbed form of the oscillator can now be written as:

$$\ddot{y} + \epsilon d\dot{y} + \beta_0 + \omega_0^2 y + \epsilon\beta_2 y^2 + \epsilon\beta_3 y^3 = \epsilon F_0\cos\omega t. \quad (11)$$

Using the method of multiple scales, we assume a solution of the form

$$y = y_0(T_0, T_1) + \epsilon y_1(T_0, T_1) + \ldots, \quad (12)$$

The first and second order time derivatives of the solution are given as:

$$\frac{d}{dt} = D_0 + \epsilon D_1 + \ldots, \quad \frac{d^2}{dt^2} = D_0^2 + 2\epsilon D_0 D_1 + \ldots, \quad (13)$$

where $D_n = \frac{\partial}{\partial T_n}$ and $T_n = \epsilon^n t$ with $0 \le \epsilon \le 1$.

Substituting Eq. (12) and Eq. (13), into Eq. (11), and equating coefficients of $\epsilon^0$ and $\epsilon^1$ separately to zero, we have

$$\epsilon^0: \quad D_0^2 y_0 + \omega_0^2 y_0 + \beta_0 = 0, \quad (14)$$

$$\epsilon^1: \quad D_0^2 y_1 + \omega_0^2 y_1 = -2D_0 D_1 y_0 - dD_0 y_0 - \beta_2 y_0^2 - \beta_3 y_0^3 + F_0\cos(\omega_0 T_0 + \sigma T_1). \quad (15)$$

The general solution of Eq. (14) can be expressed as:

$$y_0 = A(T_1)e^{j\omega_0 T_0} + \bar{A}(T_1)e^{-j\omega_0 T_0} - \frac{\beta_0}{\omega_0^2}, \quad (16)$$

where $\bar{A}$ is the complex conjugate of $A$. Inserting Eq. (16) into Eq. (15), we obtain:

$$D_0^2 y_1 + \omega_0^2 y_1 = \underbrace{\left[-2j\omega_0 A' - jd\omega_0 A + \frac{2A\beta_0\beta_2}{\omega_0^2} - 3A^2\bar{A}\beta_3 - \frac{3A\beta_0^2\beta_3}{\omega_0^4}\right]e^{j\omega_0 T_0}}_{\text{Secular Term}} + \underbrace{\frac{F_0}{2}e^{j\sigma T_1}e^{j\omega_0 T_0}}_{\text{Secular Term}} + \text{NST} + \text{CC} + \text{Constant terms}. \quad (17)$$

where CC represents the complex conjugate of the preceding terms, NST representing the non-secular terms:

$$\text{NST} = \left[-\beta_2 A^2 + \frac{3A^2\beta_0\beta_3}{\omega_0^2}\right] e^{2j\omega_0 T_0} - \beta_3 A^3 e^{3j\omega_0 T_0}, \quad (18)$$

and the Constant terms are given by

$$\text{Constant terms} = -2A\bar{A}\beta_2 + \frac{6A\bar{A}\beta_0\beta_3}{\omega_0^2} - \frac{\beta_0^2\beta_2}{\omega_0^4} + \frac{\beta_0^3\beta_3}{\omega_0^6}. \quad (19)$$

To obtain the expression for the primary resonance, we need to equate the secular terms in Eq. (17) to zero;

$$-2j\omega_0 A' - jd\omega_0 A + \frac{2A\beta_0\beta_2}{\omega_0^2} - 3A^2\bar{A}\beta_3 - \frac{3A\beta_0^2\beta_3}{\omega_0^4} + \frac{F_0}{2}e^{j\sigma T_1} = 0. \quad (20)$$

We choose

$$A(T_1) = \frac{1}{2}a(T_1)e^{jb(T_1)}, \quad (21)$$

where $a(T_1)$ and $b(T_1)$ represent the amplitude and phase respectively. Substituting Eq. (21) into Eq. (20) and separating the real and imaginary parts, then,

$$a' = -\frac{d}{2}a + \frac{F_0}{2\omega_0}\sin\delta, \quad (22)$$

$$a\delta' = a\sigma - \frac{3\beta_3}{8\omega_0}a^3 + \frac{\beta_0\beta_2}{\omega_0^3}a - \frac{3\beta_0^2\beta_3}{2\omega_0^5} + \frac{F_0}{2\omega_0}\cos\delta, \quad (23)$$

where $\delta = \sigma T_1 - b$, and $b' = \sigma - \delta'$. Eliminating $\delta$ from (22) and (23), we have the frequency-response equation given by

$$\frac{d^2}{4}a_0^2 + a_0^2\left(\sigma - \frac{3\beta_3}{8\omega_0}a_0^2 + \frac{\beta_0\beta_2}{\omega_0^3} - \frac{3\beta_0^2\beta_3}{2\omega_0^5}\right)^2 = \frac{F_0^2}{4\omega_0^2}, \quad (24)$$

where $a_0$ is the stationary state value of $a$. We solved Eq. (24) using the Newton-Raphson algorithm. Figure 1 presents the primary resonance response of the sTW oscillator for the six diatomic molecules whose properties are listed in Table I. Notably, $I_2$ and $Cl_2$ show the largest primary resonance amplitudes, while CO and $O_2$ exhibit the lowest. One might therefore be tempted to attribute resonance amplitude to molecular mass, as $I_2$ and $Cl_2$ are among the heaviest molecules. However, $H_2$, despite being the lightest molecule, shows a larger resonance amplitude than the heavier CO and $O_2$, suggesting that factors beyond mass are influential. A key factor appears to be the dissociation energy ($V_0$), with molecules that have lower $V_0$, such as $I_2$, $Cl_2$, and $H_2$, generally resonating more strongly. This trend is consistent with a lower dissociation energy correlating with a less rigid bond, making these molecules more responsive to external excitation. Conversely, the low resonance amplitude of CO, for instance, could be attributed to its high $V_0$, which indicates a stiffer bond that is more resistant to excitation. Additionally, $I_2$ and $Cl_2$ are halogens, with comparatively long bond lengths and high polarizability, further enhancing their response. Figs. 2 and 3 extend this analysis by showing the effects of the external force amplitude $F_0$ and other spectroscopic parameters $V_0$, $b_h$, and $c_h$. In all the frequency-response plots, clear evidence for dynamical hysteresis can be seen, accompanied by jump phenomenon.

Figures 2 and 3 show how the external force amplitude ($F_0$) and the spectroscopic parameters ($V_0$, $b_h$, and $c_h$) influence the primary resonance of the $H_2$ diatomic molecule. In Fig. 2, variations in $F_0$ and $V_0$ lead to remarkable nonlinear behaviors, such as dynamical hysteresis and bistability, with multiple stable states and rapid transitions. For example, with $F_0 = 4.0$, a hysteresis loop develops for detuning parameter ($\sigma$) values between 2.0 and 7.0, displaying jump phenomena within this range. Increasing $F_0$ not only raises the amplitude of the primary resonance but also broadens the resonance frequency bandwidth, allowing the system to maintain high amplitude responses over a wider range of $\sigma$. Conversely, increasing dissociation energy ($V_0$) tends to reduce the amplitude of the primary resonance, indicating a stiffer bond that is less responsive to external forces.

Figure 3 shows the effects of the potential function optimization parameters $c_h$ and $b_h$ on the primary resonance amplitude $a_0$ of the $H_2$ diatomic molecule. In Fig. 3(a), varying the optimization parameter $c_h$ significantly affects the resonance amplitude. Lower values of $c_h$ (from 0.2 to $-0.2$) provide higher peak amplitudes, enhancing the molecules's response. Higher $c_h$ values expand the frequency bandwidth across which hysteresis occurs, with $c_h = 0.2$ displaying a wide hysteresis spanning from $\sigma = 2$ to $\sigma = 8$, while lower values reduce or eliminate hysteresis. In Fig. 3(b), decreasing $b_h$ from 2.5 to 1.5 increases the peak amplitude while decreasing the hysteresis frequency range. For $b_h = 2.5$, hysteresis spanns between $\sigma = 2.5$ and $\sigma = 10$, while smaller $b_h$ values reduced the nonlinear effect. Thus, both $c_h$ and $b_h$ have a considerable impact on the amplitude and hysteresis regime of the primary resonance.

### B. Superharmonic Resonances

For superharmonic resonances, the amplitude of the external forcing is large and of the order $F = \epsilon^0 F_0$. Using the method of multiple scales and equating coefficients of $\epsilon^0$ and $\epsilon^1$ separately to zero, we have

$$\epsilon^0: \quad D_0^2 y_0 + \omega_0^2 y_0 + \beta_0 = F_0\cos\omega t, \quad (25)$$

$$\epsilon^1: \quad D_0^2 y_1 + \omega_0^2 y_1 = -2D_0 D_1 y_0 - dD_0 y_0 - \beta_2 y_0^2 - \beta_3 y_0^3. \quad (26)$$

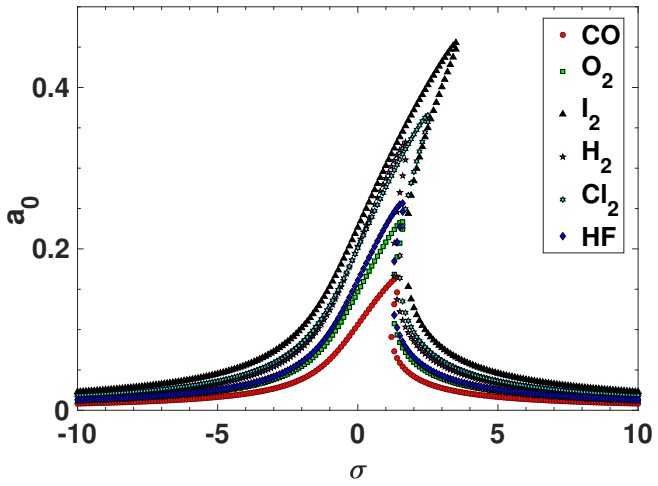


FIG. 1. Primary resonance of the sTW oscillator for $\delta_0 = 1.0$, $F_0 = 2.0$ using the parameters for six different diatomic molecule

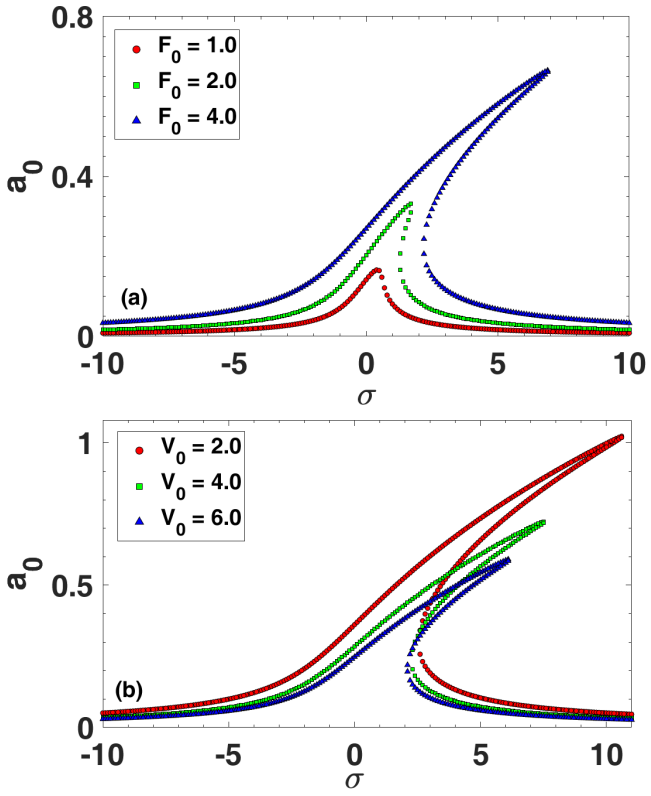


FIG. 2. Effect of (a) external force amplitude, $F_0$ and (b) $V_0$ on the primary resonance for $\delta_0 = 1.0$ using the parameters for the $H_2$ diatomic molecule.

The general solution of Eq. (25) is of the form:

$$y_0 = A(T_1)e^{j\omega_0 T_0} + \bar{A}(T_1)e^{-j\omega_0 T_0} + Be^{j\omega T_0} + Be^{-j\omega T_0} - \frac{\beta_0}{\omega_0^2}, \quad (27)$$

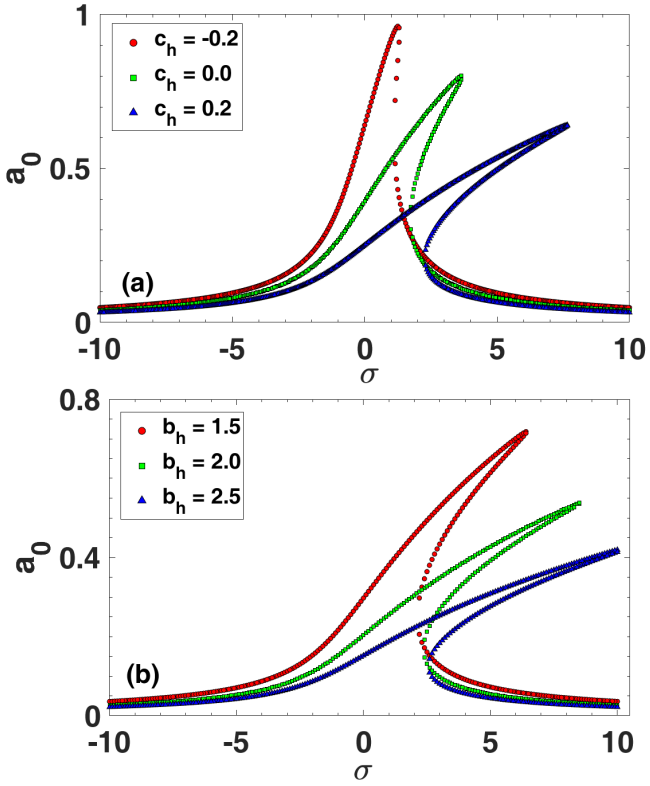


FIG. 3. Effect of (a) $c_h$ and (b) $b_h$ on the primary resonance for $\delta_0 = 1.0$ using the parameters for the $H_2$ diatomic molecule.

where $\bar{A}$ is the complex conjugate of $A$ and $B = \frac{F_0}{2(\omega_0^2 - \omega^2)}$. Inserting Eq. (27) into Eq. (26), we obtain, after some algebraic manipulations:

$$\begin{aligned}
D_0^2 y_1 + \omega_0^2 y_1 = &\left[-2j\omega_0 A' - jd\omega_0 A + \frac{2A\beta_0\beta_2}{\omega_0^2}\right. \\
&\left. -\beta_3\left(6AB^2 + 3A^2\bar{A} + \frac{3A\beta_0^2}{\omega_0^4}\right)\right]e^{j\omega_0 T_0} \\
&+\left[-jd\omega B + \frac{2B\beta_0\beta_2}{\omega_0^2} - \beta_3\left(3B^3 + 6A\bar{A}B\right.\right. \\
&\left.\left. +\frac{3B\beta_0^2}{\omega_0^4}\right)\right]e^{j\omega T_0} + \left[\frac{3B^2\beta_0\beta_3}{\omega_0^2} - B^2\beta_2\right]e^{2j\omega T_0} \\
&-B^3\beta_3 e^{3j\omega T_0} - 2AB\beta_2 e^{j(\omega+\omega_0)T_0} - 2\bar{A}B\beta_2 e^{j(\omega-\omega_0)T_0} \\
&-3AB^2\beta_3 e^{j(2\omega+\omega_0)T_0} - 3A^2 B e^{j(\omega+2\omega_0)T_0} \\
&-3\bar{A}B^2\beta_3 e^{j(2\omega-\omega_0)T_0} - 3\bar{A}^2 B\beta_3 e^{j(\omega-2\omega_0)T_0} \\
&+\frac{6AB\beta_0\beta_3}{\omega_0^2}e^{j(\omega+\omega_0)T_0} + \frac{6\bar{A}B\beta_0\beta_3}{\omega_0^2}e^{j(\omega-\omega_0)T_0} \\
&+\text{NST} + \text{CC} + \text{Constant terms}, \quad (28)
\end{aligned}$$

where CC represents the complex conjugate of the preceding terms, NST representing the non-secular terms

$$\text{NST} = \left[-\beta_2 A^2 + \frac{3A^2\beta_0\beta_3}{\omega_0^2}\right] e^{2j\omega_0 T_0} - A^3\beta_3 e^{3j\omega_0 T_0}, \quad (29)$$

and the Constant terms are given by

$$\text{Constant terms} = -\beta_2\left(2B^2 + 2A\bar{A} + \frac{\beta_0^2}{\omega_0^4}\right) + \beta_3\left(\frac{\beta_0^3}{\omega_0^6} + \frac{6B^2\beta_0}{\omega_0^2} + \frac{6A\bar{A}\beta_0}{\omega_0^2}\right). \quad (30)$$

We can see from Eq. (28) that the system can exhibit some superharmonic states.

For the 1:2 superharmonic state, we substitute $2\omega = \omega_0 + \epsilon\sigma$ into Eq. (28) and set the secular terms to zero, so that

$$-2j\omega_0 A' - jd\omega_0 A + \frac{2A\beta_0\beta_2}{\omega_0^2} - \beta_3\left(6AB^2 + 3A^2\bar{A} + \frac{3A\beta_0^2}{\omega_0^4}\right) + \left[\frac{3B^2\beta_0\beta_3}{\omega_0^2} - B^2\beta_2\right] e^{j\sigma T_1} = 0. \quad (31)$$

By substituting the polar form of $A$ given by

$$A(T_1) = \frac{1}{2}a(T_1)e^{jb(T_1)}, \quad (32)$$

and separating the real and imaginary parts, we have

$$a' = -\frac{d}{2}a + \frac{\Delta_1}{\omega_0}\sin\delta, \quad (33)$$

$$a\delta' = a\sigma + \frac{\beta_0\beta_2}{\omega_0^3}a - \beta_3\left(\frac{3B^2}{\omega_0}a + \frac{3}{8\omega_0}a^3 + \frac{3\beta_0^2}{2\omega_0^5}a\right) + \frac{\Delta_1}{\omega_0}\cos\delta, , \quad (34)$$

where $\Delta_1 = \frac{3B^2\beta_0\beta_3}{\omega_0^2} - B^2\beta_2$ and $\delta = \sigma T_1 - b$. Eliminating $\delta$ from Eq. (33) and Eq. (34), we get the following frequency response equation

$$\frac{d^2}{4}a_0^2 + a_0^2\left(\sigma + \frac{\beta_0\beta_2}{\omega_0^3} - \beta_3\left(\frac{3B^2}{\omega_0} + \frac{3}{8\omega_0}a_0^2 + \frac{3\beta_0^2}{2\omega_0^5}\right)\right)^2 = \left(\frac{3B^2\beta_0\beta_3}{\omega_0^3} - \frac{B^2\beta_2}{\omega_0}\right)^2, \quad (35)$$

where $a_0$ is the stationary state value of $a$.

For the $1:3$ superharmonic state, we substitute $3\omega = \omega_0 + \epsilon\sigma$ into Eq. (28) and set the secular terms to zero, so that

$$-2j\omega_0 A' - jd\omega_0 A + \frac{2A\beta_0\beta_2}{\omega_0^2} - \beta_3\left(6AB^2 + 3A^2\bar{A} + \frac{3A\beta_0^2}{\omega_0^4}\right) - B^3\beta_3 e^{j\sigma T_1} = 0. \quad (36)$$

In this case, the frequency response equation is given by

$$\frac{d^2}{4}a_0^2 + a_0^2\left(\sigma + \frac{\beta_0\beta_2}{\omega_0^3} - \beta_3\left(\frac{3B^2}{\omega_0} + \frac{3}{8\omega_0}a_0^2 + \frac{3\beta_0^2}{2\omega_0^5}\right)\right)^2 = \frac{B^6\beta_3^2}{\omega_0^2}. \quad (37)$$

Using the Newton-Raphson algorithm for Eq. (35) and Eq. (37), the amplitude equation was iterated, plotting $a_0$ as a function of the detuning parameter $\sigma$ for different values of the spectroscopic parameters. Figs. 4 and 7 display the second- and third-order superharmonic resonance responses of the sTW oscillator for six diatomic molecules. Compared to the primary resonance in Fig. 1, the superharmonic resonances exhibit higher amplitudes and more pronounced hysteresis effects across all the molecules. $I_2$ and $Cl_2$ exhibit particularly high resonance amplitudes and broader hysteresis frequency bandwidths, suggesting increased sensitivity to nonlinear effects under superharmonic excitation. In contrast, CO and $O_2$ displayed lower amplitudes with no evidence of hysteresis under these conditions. The increased response and expanded hysteresis in superharmonic resonance are largely attributable to the high $F_0$ and the specific molecular parameters ($V_0$, $b_h$, and $c_h$). Molecules with lower $V_0$ and favorable parameter values tend to exhibit more extensive hysteresis, underscoring the role of bond flexibility and polarizability in shaping resonance behavior. In summary, superharmonic resonance shows amplification of both the amplitude and nonlinear response, indicating the complex interaction between molecular properties and external excitation forces.

In Figures 5 and 8, the second- and third-order superharmonic resonance responses of the sTW oscillator for the $H_2$ diatomic molecule are presented, showing the effects of varying the external force amplitude $F_0$ and dissociation energy $V_0$. Notably, for the second-order resonance shown in Fig. 5(a), setting $F_0 = 8.0$ promotes an enhanced hysteresis loop, indicating high sensitivity to nonlinear effects and a broader range of the detuning parameter $\sigma$ (from approximately $\sigma = 6$ to $\sigma = 16.5$) where jump phenomena occur. Similarly, in Fig. 5(b), $V_0 = 2.0$ leads to an extended hysteresis range, indicating increased bond flexibility and susceptibility to nonlinear dynamics. For the third-order resonance shown in Fig. 8, the effects are even more pronounced. For instance, at $F_0 = 15.0$ shown in Fig. 8(a), the hysteresis loop spans a wider $\sigma$ range (from approximately $\sigma = 10$ to $\sigma = 26$), indicating a heightened response of the oscillator under stronger external forcing. Likewise, $V_0 = 2.0$ in Fig. 8(b) results in substantial hysteresis, with jump phenomena observed over a wider range of $\sigma$ values than observed for higher $V_0$. These cases underscore that higher $F_0$ and lower $V_0$ values amplify the nonlinear behavior of the oscillator, making the system more responsive to superharmonic excitations and extending the range of detuning over which nonlinear effects such as hysteresis and jump phenomena are evident.

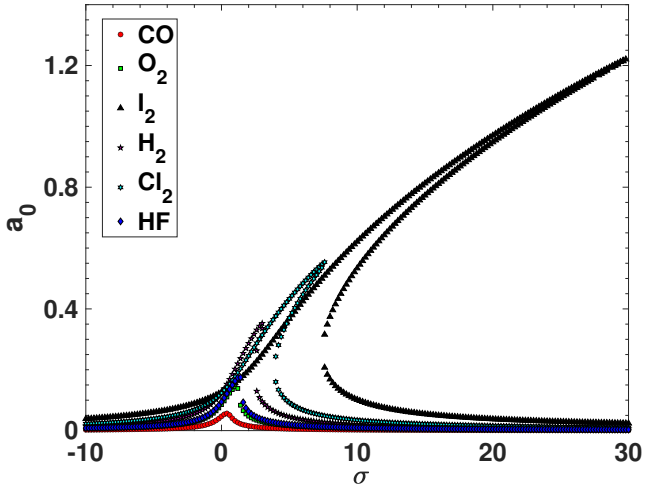


FIG. 4. Second order superharmonic resonance of sTW oscillator for $\delta_0 = 1.0$, $F_0 = 5.0$ using the parameters for six different diatomic molecules

In Figures 6 and 9, the effect of varying parameters $c_h$ and $b_h$ on the amplitude $a_0$ of the response was explored for the second and third order superharmonic resonances for the $H_2$ diatomic molecule, with $\delta_0 = 1.0$. Evidently, these potential optimization parameters have a rather filtering impact on the response amplitude, with no appearance of hysteresis or discontinuous jumps. Figs. 6(a) and 9(a) show the influence of $c_h$ on the second and third order superharmonic resonances, respectively. Varying $c_h$ from $-0.2$ to 0.2 enhances the peak amplitude $a_0$, with no noticeable jumps or discontinuities in the frequency-response curve. The absence of hysteresis or jump phenomena suggests that the response is smooth and stable, with no abrupt shifts as $\sigma$ changes.

Similarly, in Figs. 6(b) and 9(b), which show the effect of $b_h$ on the second and third order superharmonic resonances, we found a slight increase in the peak amplitude as $b_h$ decreases from 2.5 to 1.5. This change, like the effect of $c_h$, is not pronounced, indicating that fluctuations in $b_h$ have a little influence on the resonance amplitude. Furthermore, the resonance curves stay smooth and continuous throughout the parameter range, with no occurrence of hysteresis with variations in $b_h$. In summary, both $c_h$ and $b_h$ have only marginal effects on the amplitudes of the second and third order superharmonic resonances, producing only modest changes in peak heights. The absence of hysteresis for this case is indicative of a stable, continuous response, implying that the system's behaviour is adaptable to changes in these parameters, resulting in smooth amplitude dynamics.

## IV. BIFURCATION ANALYSIS

To comprehend the complex resonance features more deeply, we now carry out a numerical bifurcation analysis of the system's structures. The sTW oscillator can

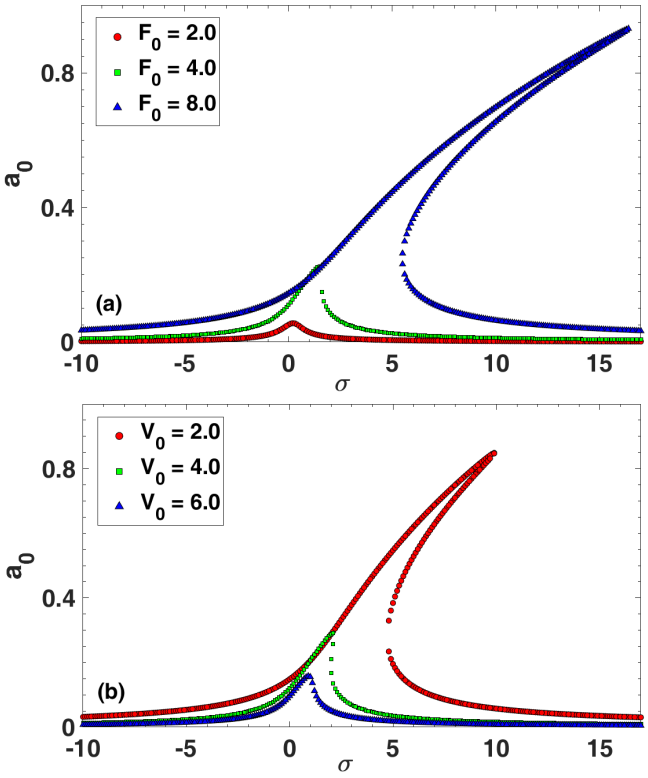


FIG. 5. Effect of (a) external force amplitude, $F_0$ and (b) $V_0$ on the second order superharmonic resonance for $\delta_0 = 1.0$ using the parameters for the $H_2$ diatomic molecule.

be written as a non-autonomous first order differential equations of the form

$$\dot{x} = u,$$
$$\dot{u} = -\delta u - \frac{dV}{dx} + f\cos\omega t. \tag{38}$$

Without the external forcing i.e. $f = 0$, we find that the only fixed point of the model Eq. (38) is $X = (x, u) = (r_e, 0)$ and the Jacobian matrix $J$ evaluated at this fixed point is given by

$$J = \begin{pmatrix} 0 & 1 \\ Q & -\delta \end{pmatrix} \tag{39}$$

where

$$Q = -\frac{V_0 b_h^2}{(1-c_h)^2},$$

The eigenvalues of the Jacobian matrix (Eq. (39)) are obtained from the corresponding characteristic equation as

$$\frac{1}{2}\left(-\delta + \sqrt{d^2 + 4Q}\right).$$

The fixed point $(r_e, 0)$ is a stable sink or spiral for $\delta^2 > 4|Q|$ and $\delta^2 < 4|Q|$ respectively when $\delta > 0$. For $\delta <$

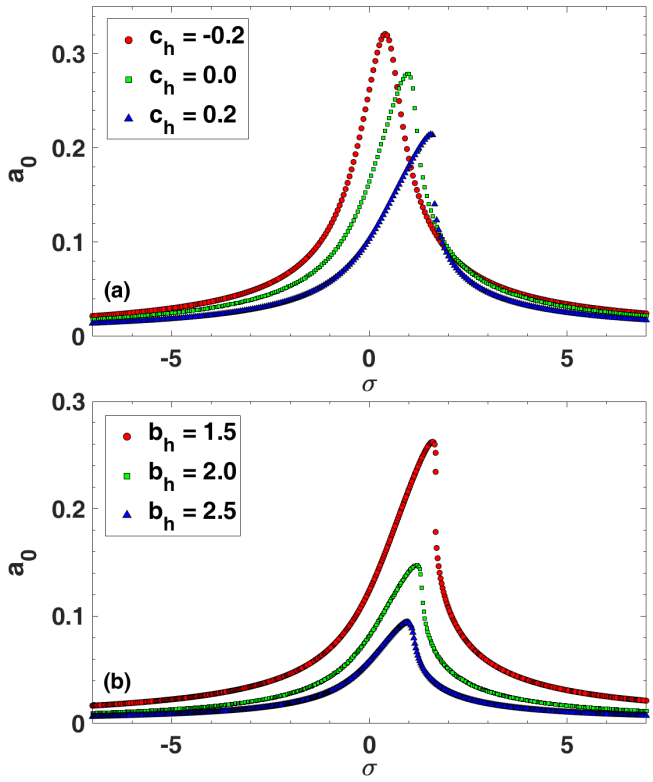


FIG. 6. Effect of (a) $c_h$ and (b) $b_h$ on the second order superharmonic resonance for $\delta_0 = 1.0$ using the parameters for the $H_2$ diatomic molecule.

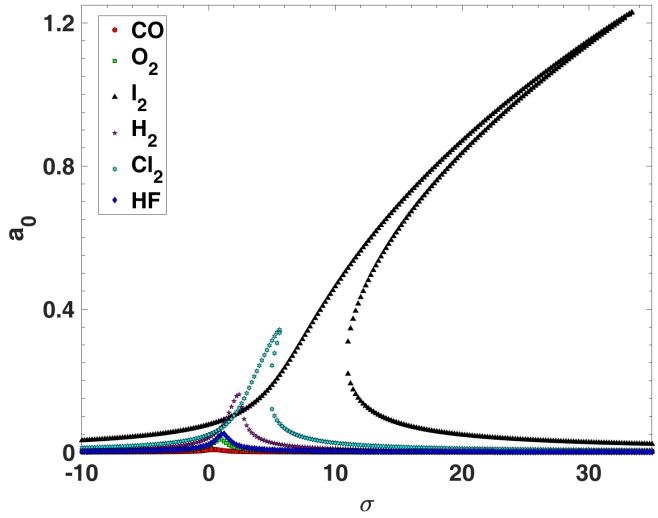


FIG. 7. Third order superharmonic resonance of sTW oscillator for $\delta_0 = 1.0$, $F_0 = 8.0$ using the parameters for six different diatomic molecules

0, it becomes an unstable sink or spiral for $\delta^2 > 4|Q|$ and $\delta^2 < 4|Q|$ respectively. In addition, the fixed point $(r_e, 0)$ is hyperbolic. Hence, the model is topologically and structurally stable [95–97]. Since it is the only fixed point of the model, local stability through linearization and calculation of eigenvalues should suffice.

Now, in the case when $f \neq 0$, the model (Eq. (38)) can be rewritten as a first-order autonomous ordinary differential equation of the following form:

$$\begin{aligned} \dot{x} &= u, \\ \dot{u} &= -\delta u - \frac{dV}{dx} + f\cos\omega\theta, \\ \dot{\theta} &= 1. \end{aligned} \tag{40}$$

where $(x, u, \theta) \in \mathbb{R}^2 \times S^1$, $(x, u) \in \mathbb{R}^2$ is the two-dimensional Euclidean space, $\theta \in S^1$ represent points on the unit circle of length $T = 2\pi/\omega$ and $T$ is the period of the external forcing [86, 98, 99]. For similar forced systems, we know that the fixed point $(r_e, 0)$ will generate hyperbolic circular orbits in the phase space $\mathbb{R}^2 \times S^1$. Furthermore, based on the invariant manifold theorem [100, 101], such circular orbits persist for all $f \neq 0$, losing merely their circularity while retaining the same fundamental qualitative properties [95, 98].

In vector notation, Eq. (40) is of the form $\dot{X} = \phi(X, \mu)$, where $\phi(X, \mu)$ is an autonomous vector field, $X = (x, u, \theta)$ represents the phase space $\mathbb{R}^2 \times S^1$ and $\mu = (\delta, f, \omega, V_0, c_h, b_h)$ is the vector element for the parameter space. The dependences of the model on the sTW potential parameters $V_0$,$c_h$ and $b_h$ are implied from the potential gradient term $dV/dx$.

In our numerical analysis, we consider the global Poincaré map $P : \Sigma \to \Sigma$ [86, 98],

$$x_p = (x, u) \to P(x_p) = \phi^T|_\Sigma(x, u, c),$$

where $c$ is a constant determining the location of the Poincaré cross-section on which the coordinates $(x, u)$ of the attractor are expressed, and the Poincaré plane $\Sigma$ is given by

$$\Sigma = \{(x, u, \theta) \in \mathbb{R}^2 \times S^1 \quad |\theta = c = 0\}.$$

For the numerical simulations, the sTW oscillator equation (1), rewritten as Eq. (38), is solved numerically by implementing a fourth-order Runge-Kutta algorithm with the initial conditions $x(0) = r_e + 0.5$, $u(0) = \dot{x}(0) = 0$, except otherwise indicated [102, 103].

Bifurcation analysis is a mathematical and computational technique used to understand how the behaviour of dynamical systems changes as parameters are changed. When a control parameter $\mu = (\delta, f, \omega, V_0, c_h, b_h)$ of the model is varied, we want to know what key qualitative changes occur in the model solution. To generate the bifurcation diagrams, one model parameter is changed in very small equidistant steps while the other parameters remain constant. The bifurcation diagrams are obtained after the first 800 cycles of the driving period $T$ have been discarded as transients, to ensure that the system has reached a steady state solution. The corresponding $x, u$ points on the bifurcation diagram are plotted by using the previous step's final value as the initial condition

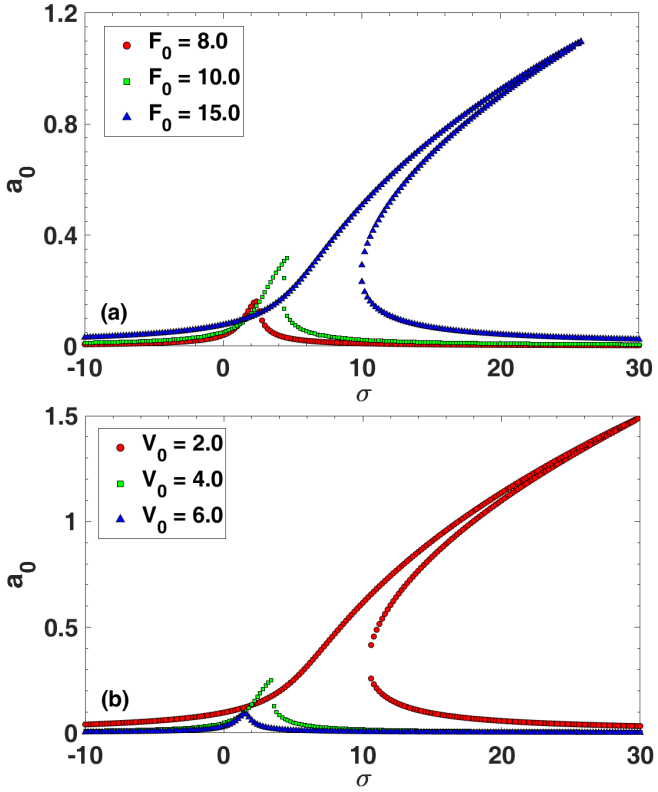


FIG. 8. Effect of (a) external force amplitude, $F_0$ and (b) $V_0$ on the third order superharmonic resonance for $\delta_0 = 1.0$ using the parameters for the $H_2$ diatomic molecule.

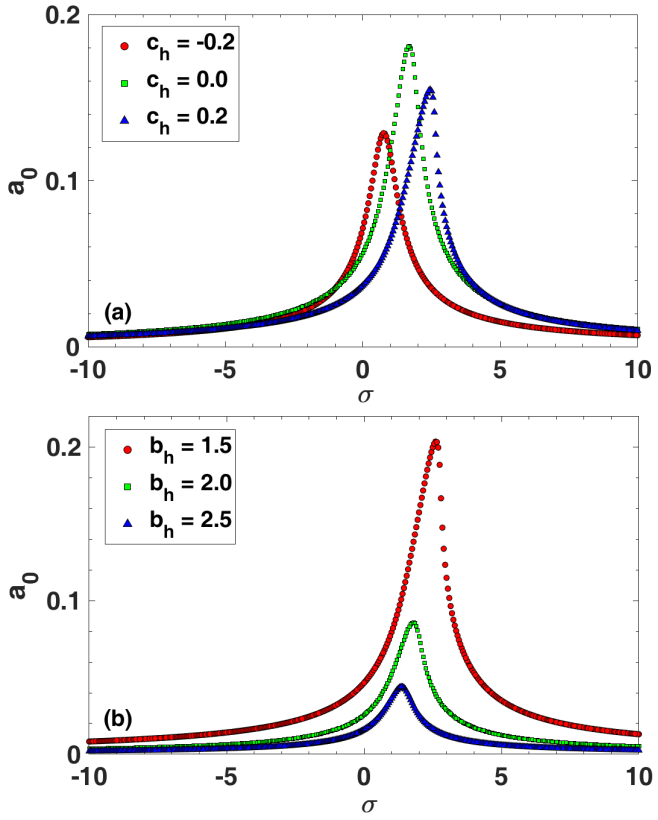


FIG. 9. Effect of (a) $c_h$ and (b) $b_h$ on the third order superharmonic resonance for $\delta_0 = 1.0$ using the parameters for the $H_2$ diatomic molecule.

for the next step. The results are presented and discussed in the following figures.

Figure 10 shows the bifurcation diagram in panel (a) and maximal Lyapunov exponent in (b) for the sTW oscillator with the parameter $f$ ranging from 1.0 to 3.5. The bifurcation diagram initially exhibits stable, periodic behaviour for the lower $f$ values, then switches to chaotic dynamics interspersed with periodic windows as $f$ grows. A period-1 attractor exists from $f = 0$ to about 1.108. This attractor undergoes a period-doubling bifurcation, resulting in a period-2 attractor for $f$ values between 1.108 and 1.657. Subsequent period-doubling bifurcations create chaotic attractors around $f = 1.754$ (Fig. 11(a).

At $f \approx 2.116$, a boundary crisis triggers a tangent bifurcation, generating a period-3 attractor (Fig. 11(b)). The phase portrait just before the crisis at the critical value $f = 2.116$ is shown in Fig. 12(a), while the period-3 attractor immediately following the crisis at $f = 2.12$ is depicted in Fig. 12(b). This period-3 attractor undergoes further period-doubling until chaotic behavior re-emerges at around $f = 2.23$. An interior crisis at $f = 2.267$ subsequently induces intermittency, where the orbit alternates between two narrow chaotic bands (Fig. 11(b)).

Further bifurcations lead to additional periodic windows, each initiated by boundary crises, followed by period-doubling events that culminate in narrow chaotic

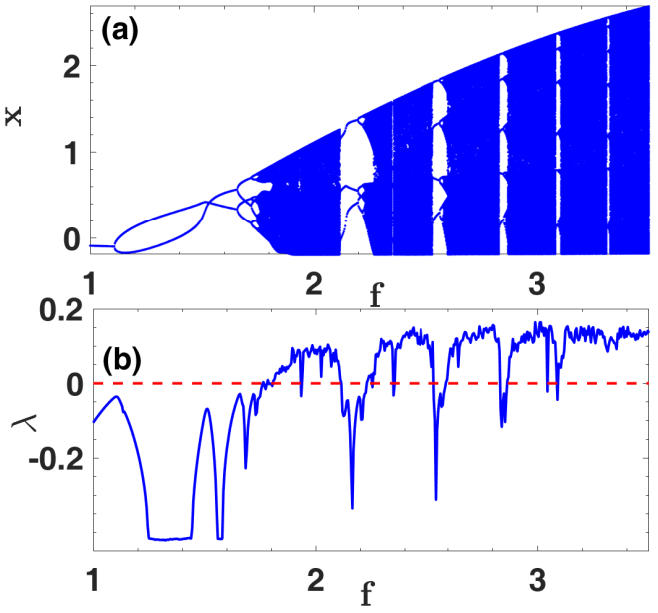


FIG. 10. (a) Bifurcation diagram of the sTW oscillator, illustrating the evolution of the system's behavior with respect to $f$. (b) Corresponding maximal Lyapunov exponent as a function of $f$, highlighting regions of chaos (positive values) and stability (negative values). Other parameters are fixed at $b_h = 1.0$, $c_h = 0.25$, $r_e = 0$, $V_0 = 1.0$, $\omega = 2.0$, $\delta = 0.8$.

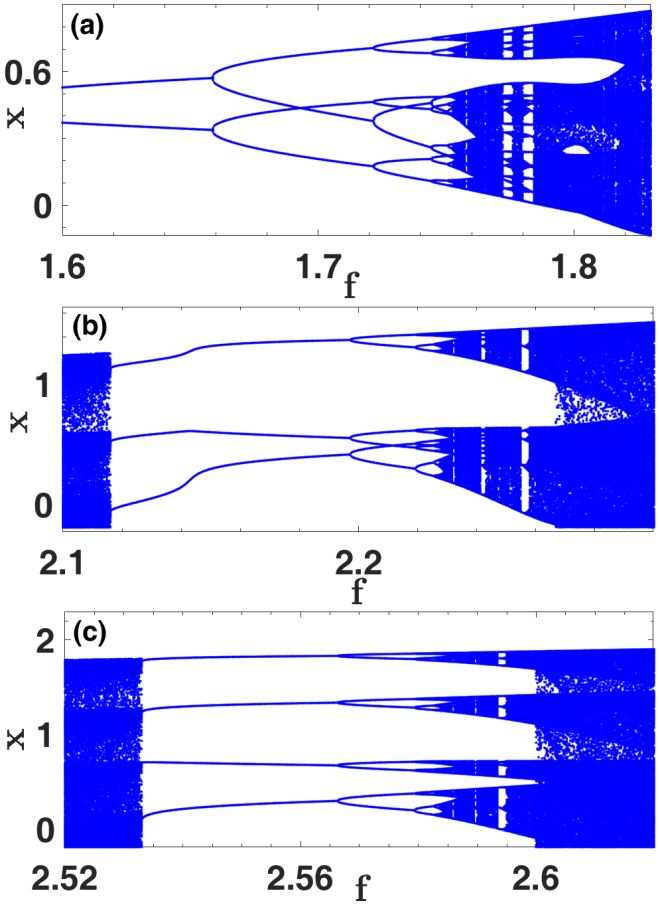


FIG. 11. Enlarged windows of the sTW oscillator bifurcation diagram shown in Fig. 10.

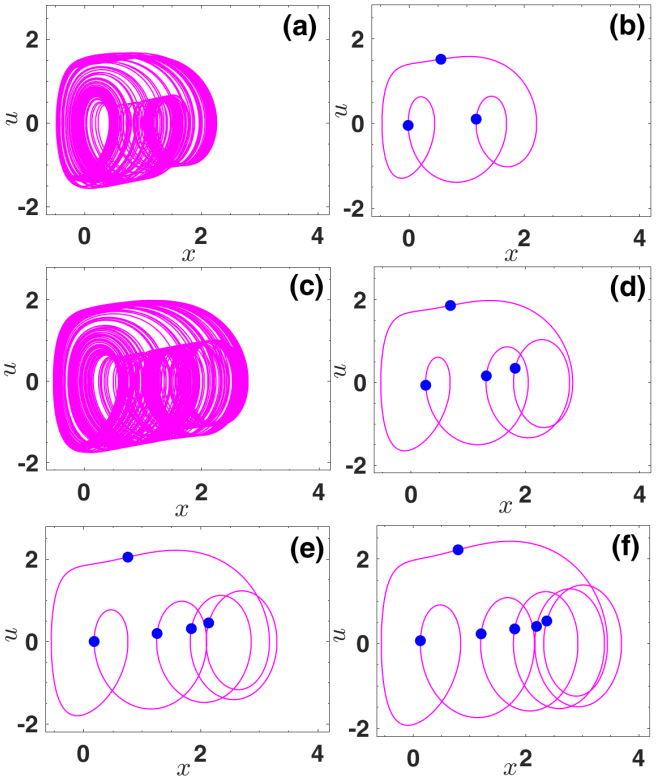


FIG. 12. Phase portraits of the sTW oscillator for selected values of $f$ from Fig. 10, illustrating the system's dynamic behavior at: (a) $f = 2.11$ (chaotic), (b) $f = 2.12$ (period-3), (c) $f = 2.52$ (chaotic), (d) $f = 2.55$ (period-4), (e) $f = 2.597$ (chaotic), (f) $f = 2.601$ (chaotic). The blue dots represent the corresponding points in the Poincaré section

bands and terminated in an attractor-merging crisis as $f$ increases. Notably, each new periodic attractor in these windows has a higher period than its predecessor. For instance, a period-4 attractor is formed at a boundary crisis event at $f = 2.533$ and terminates at an attractor-merging crisis at $f = 2.60$, where four narrow band chaotic attractors merge into a larger chaotic attractor. The phase portrait just before the boundary crisis at $f = 2.52$ is shown in Fig. 12(c), while the period-4 attractor at $f = 2.55$ is displayed in Fig. 12(d). Figs. 12(e) and 12(f) represent the phase portraits just before and after the attractor-merging crisis at $f = 2.60$. For clarity, the nature and structure of the attractor-merging crisis at $f = 2.60$ were further elucidated using the Poincaré section shown in Fig. 13, which clearly shows the merging of four narrow-band attractors into a larger one. A period-5 attractor appears for $f$ values lying between approximately 2.833 and 2.851, and a period-6 attractor emerges for $f$ values between 3.085 and 3.094.

Figure 12 shows phase portraits that visually demonstrate the system's dynamics as $f$ rises. These images show how the orbit widens with increasing $f$, indicating the system's transition from limited, periodic behaviour to broader trajectories. For example, at the value $f = 2.12$, the period-3 attractor in Fig. 12(b) depicts a more compact orbit, whereas the period-4 attractor observed at $f = 2.55$ (Fig. 12(b)) indicates a substantial expansion. This sequence continues with the higher-period attractors and chaotic bands, illustrating the increased complexity and amplitude of oscillations as $f$ increases. The Lyapunov exponent plot in Fig. 10 confirms these bifurcation sequences. Regions with negative exponents correspond to stable behavior, while positive exponents indicate chaos, marked by the exponential divergence of nearby trajectories. This plot underscores the complex interplay between order and chaos as $f$ varies, offering valuable insights into the stability and dynamical behavior of the sTW oscillator under external forcing.

Figure 14(a) displays the bifurcation diagram with the corresponding maximal Lyapunov exponent in (b) for the system with parameters $V_0 = 4.0$ and $\omega = 0.5$, as the parameter $f$ varies from 2.5 to 4.0. At lower $f$ values, the system exhibits a period-1 attractor until about $f \approx 2.71$, when a sudden transition to chaos takes place, implies a Pomeau-Manneville intermittency route to chaos. Between $f = 2.756$ and $f = 3.174$, the system exhibits multistability, with multiple coexisting attractors. For $f = 2.756$ to $f \approx 2.78$, a period-1 orbit and a chaotic

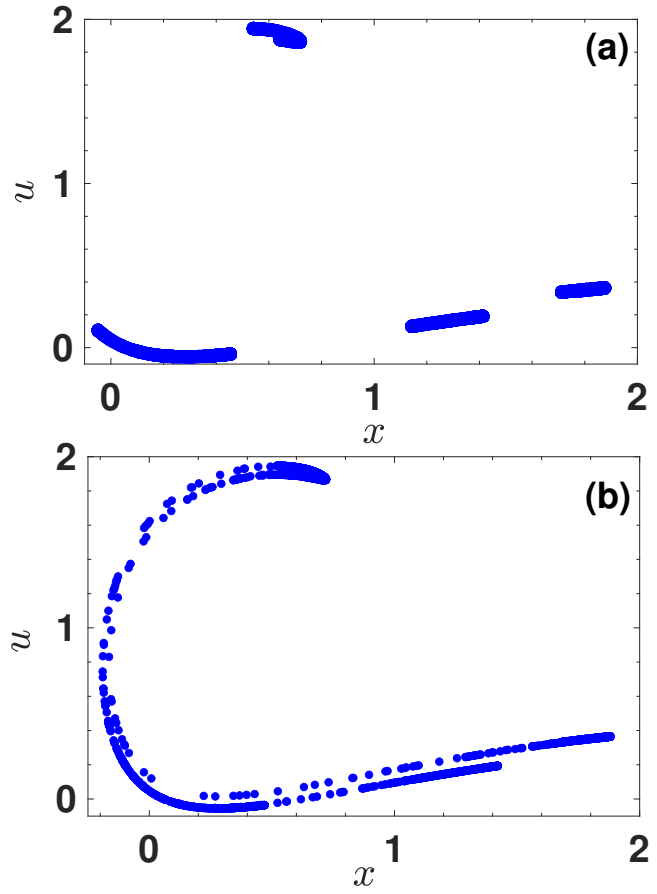


FIG. 13. Poincaré section of the sTW oscillator corresponding to the attractor-merging crisis shown in Figs. 12(e) and (f): (a) $f = 2.597$ (narrow 4-band chaotic attractor just before crisis), (b) $f = 2.601$ (chaotic attractor just after crisis).

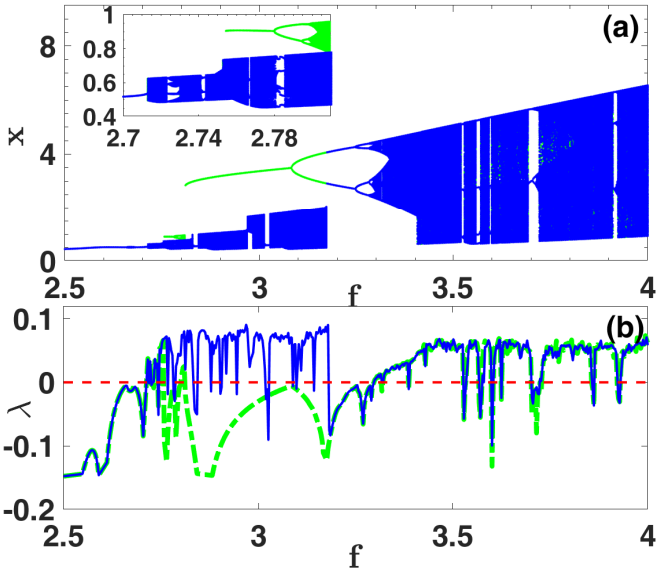


FIG. 14. (a) Bifurcation diagram of the sTW oscillator, illustrating the evolution of the system's behavior with respect to $f$. (b) Corresponding maximal Lyapunov exponent as a function of $f$: solid blue line for blue attractor branch and green-dashed line for green attractor branch, highlighting regions of chaos (positive values) and stability (negative values). The inset in (a) shows a zoom of the driving frequency regimes for which coexisting chaotic attractors exist in the neighborhood of $f = 2.8$. Other parameters are fixed at $b_h = 1.0$, $c_h = 0.25$, $r_e = 0$, $V_0 = 4.0$, $\omega = 0.5$, $\delta = 0.8$.

attractor coexist. A similar coexistence of period-1 and chaotic attractors is also observable for $f$ values lying between 2.81 and 3.082. Again, coexisting chaotic attractors are present between $f \approx 2.80$ and $f \approx 2.81$. Finally, from $f = 3.082$ to $f = 3.174$, a period-2 orbit and a chaotic attractor coexist. The basins of attraction for these coexisting states are shown in Fig. 15, where panel (a) illustrates the basins for coexisting chaotic attractors at $f = 2.805$, and panel (b) shows the basins for coexisting period-2 (blue) and chaotic attractors at $f = 3.15$. These basins highlight the system's multistability, where different initial conditions ($x_0$ and $u_0$) result in convergence to distinct attractors. The fractal and striped patterns in Figs. 15(a) and (b) respectively, suggests that the initial condition space alternates between regions of attraction for the periodic and chaotic states, demonstrating the system's extreme sensitivity to initial conditions. The phase portraits corresponding to these coexisting attractors are presented in Fig. 16. Figs. 16(a) and (b) show the phase portraits for the coexisting chaotic attractors at $f = 2.805$, while Figs. 16(c) and (d) depict the period-2 and chaotic attractors at $f = 3.15$ for two closely chosen initial conditions.

As $f$ increases, an interior crisis occurs in the neighborhood of $f = 3.406$, characterized by a sudden expansion in the chaotic domain. This event follows a period-doubling sequence from $f \approx 3.246$ to $f \approx 3.294$. The phase portrait just before the interior crisis at $f = 3.4$ is shown in Fig. 16(e), while Fig. 16(f) presents the post-crisis portrait at $f = 3.42$. Notably, the orbit in Fig. 16(f) intermittently visits the pre-crisis regime depicted in Fig. 16(e), indicating the presence of crisis-induced intermittency. Fig. 17 presents the Poincaré sections corresponding to the phase portraits in Fig. 16, providing further illustrations of the coexisting chaotic attractors at $f = 2.805$, the coexisting period-2 and chaotic attractors at $f = 3.15$, and the interior crisis at $f = 3.4$.

Furthermore, there are periodic windows throughout the bifurcation structure, initiated by boundary crises and terminating in period-doubling transitions to chaos. A period-3 window occurs for $f$ values between approximately 3.52 and 3.526, a period-4 window from 3.558 to 3.568, and a period-2 attractor from 3.694 to 3.704. The maximal Lyapunov exponent plot in Fig. 14(b) corroborates these observations, validating the observed transitions between periodic and chaotic dynamics as seen in the bifurcation diagram (Fig. 14(a)). Negative exponents confirm stable, periodic behavior, while positive exponents signal chaotic dynamics with exponential di-

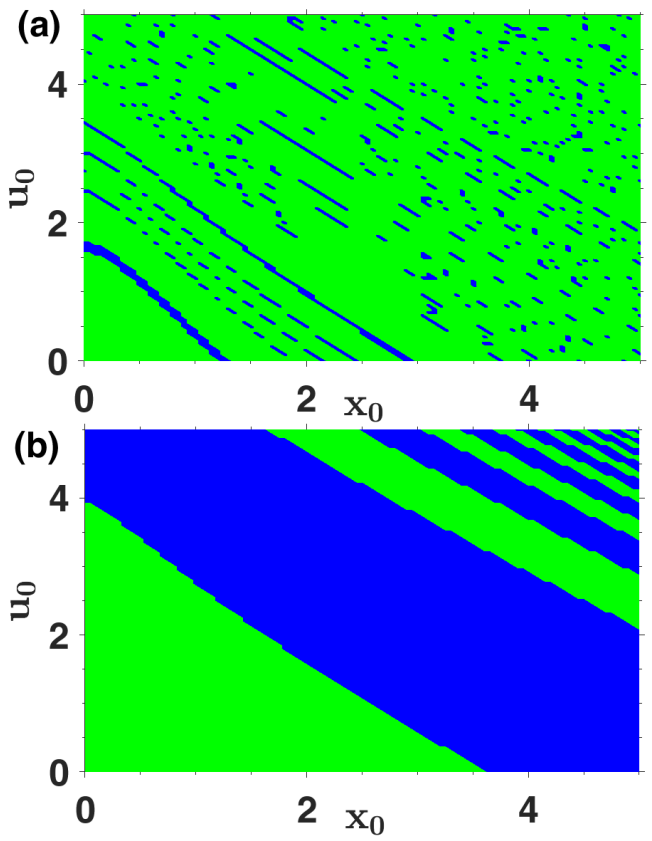


FIG. 15. Basins of attraction of the coexisting attractors in Fig. 14: (a) $f = 2.805$ (coexisting chaotic attractors); (b) $f = 3.15$ (coexisting period-2 (blue) and chaotic attractor (green)).

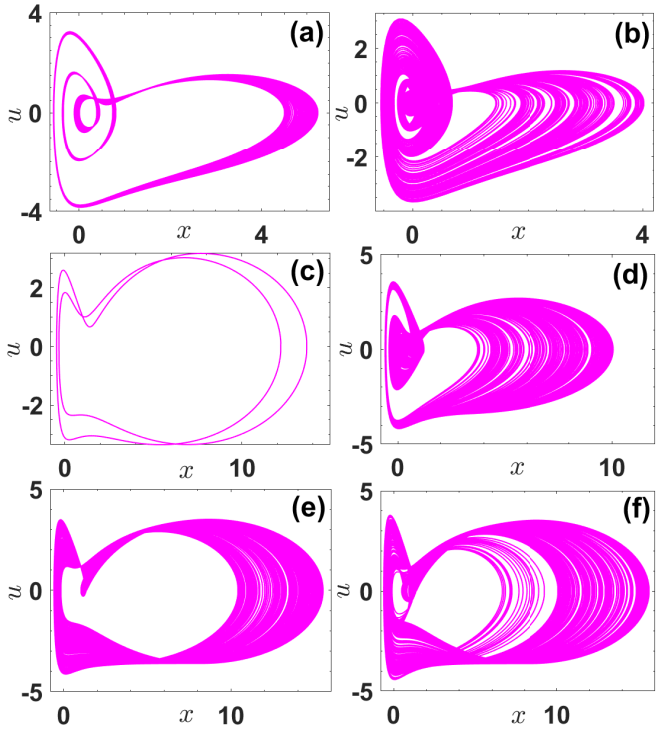


FIG. 16. Phase portraits of the sTW oscillator for selected values of $f$ from Fig. 14, illustrating the system's dynamic behavior at: (a) $f = 2.805$, $(x_0, u_0) = (1.0, 0.5)$ (chaotic) (b) $f = 2.805$, $(x_0, u_0) = (1.0, 0.53)$ (chaotic) (c) $f = 3.15$, $(x_0, u_0) = (2.0, 1.7)$ (period-2) (d) $f = 3.15$, $(x_0, u_0) = (2.0, 1.5)$ (chaotic) (e) $f = 3.4$ (chaotic), (f) $f = 3.42$ (chaotic).

vergence of trajectories.

The bifurcation diagram in Fig. 18(a) and corresponding maximal Lyapunov exponent in (b) illustrate the evolution of the state variable $u = \dot{x}$ of the sTW oscillator as the driving frequency $\omega$ varies. For clarity, an expanded portion of the bifurcation diagram from Fig. 18(a) is displayed in Fig. 19, while Fig. 20 shows the phase portraits corresponding to different $\omega$ values.

Figure 19(a) shows that the sTW oscillator initially exhibits a period-1 attractor as the external forcing frequency $\omega$ rises from zero. A saddle-node bifurcation occurs at $\omega = 0.2282$. The system then undergoes a sequence of symmetry-breaking period-doubling bifurcations between $\omega \approx 0.3116$ and $\omega \approx 0.489$. Attractor bubbling is evident for $\omega$ values between 0.489 and 0.5126. This interval includes the transformation of a period-4 attractor at $\omega = 0.485$ (Fig. 20(a)) into an asymmetrical period-8 attractor at $\omega = 0.50$ (Fig. 20(b)). This attractor bubbling, sandwiched by symmetry-breaking, is followed by another saddle-node bifurcation at $\omega = 0.5192$.

Chaotic behavior emerges for $\omega$ values from 0.525 until a boundary crisis at $\omega \approx 0.622$ leads to a period-3 attractor. The chaotic attractor just before this boundary crisis at $\omega = 0.62$ is shown in Fig. 20(c), while the post-crisis period-3 attractor at $\omega = 0.63$ is depicted in Fig. 20(d). From Fig. 19(b), three narrow chaotic bands can be seen between $\omega = 0.78$ and $\omega = 1.038$, terminating with a boundary crisis. This crisis occurs due to a collision between the chaotic attractor and the emerging period-3 orbit on its basin boundary. Fig. 19(e) depicts the chaotic attractor at $\omega = 1.02$ before this crisis, while Fig. 19(f) depicts the period-3 attractor at $\omega = 1.038$ after it. Additionally, symmetry-breaking is present between a period-doubling and a reverse period-doubling, with sudden chaotic transitions observed near $\omega \approx 1.776$. Following the chaotic transition at $\omega \approx 1.776$, the chaotic band persists until $\omega \approx 2.50$. After this, a series of reverse period-doubling events leads the system progressively from chaos to periodic order, culminating with a period-1 attractor beyond $\omega = 3.74$. The extensive chaotic region between $\omega = 1.776$ and $\omega = 2.50$, detailed in Figs. 19 (c) and (d), contains various periodic windows produced by the splitting of chaotic attractors and reverse period-doubling bifurcations. Notable attractors in these windows include a period-5 attractor from $\omega \approx 2.142$ to $\omega \approx 2.151$, a period-6 attractor from $\omega \approx 2.386$ to $\omega \approx 2.395$, a period-7 attractor from $\omega \approx 2.06$ to $\omega \approx 2.062$, and a period-8 attractor

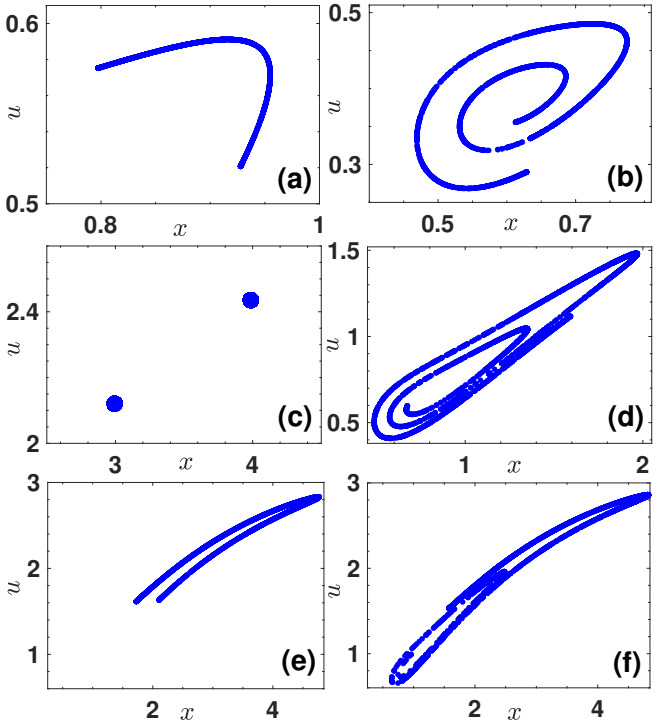


FIG. 17. Poincaré section of the sTW oscillator corresponding to the $f$ values from Fig. 16, illustrating the system's dynamic behavior at: (a) $f = 2.805$, $(x_0, u_0) = (1.0, 0.5)$ (chaotic) (b) $f = 2.805$, $(x_0, u_0) = (1.0, 0.53)$ (chaotic) (c) $f = 3.15$, $(x_0, u_0) = (2.0, 1.7)$ (period-2) (d) $f = 3.15$, $(x_0, u_0) = (2.0, 1.5)$ (chaotic) (e) $f = 3.4$ (chaotic), (f) $f = 3.42$ (chaotic).

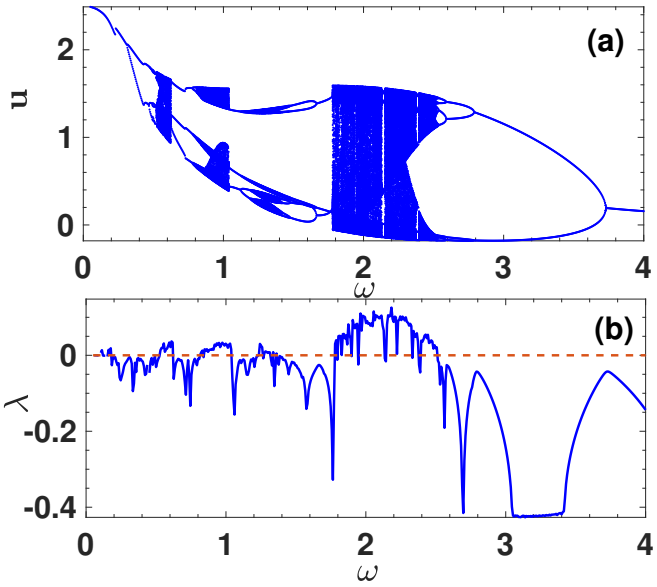


FIG. 18. (a) Bifurcation diagram of the sTW oscillator, illustrating the evolution of the system's behavior with respect to $\omega$. (b) Corresponding maximal Lyapunov exponent as a function of $\omega$, highlighting regions of chaos (positive values) and stability (negative values). Other parameters are fixed at $b_h = 1.0$, $c_h = 0.25$, $r_e = 0$, $V_0 = 1.0$, $\delta = 0.8$, $f = 2.0$.

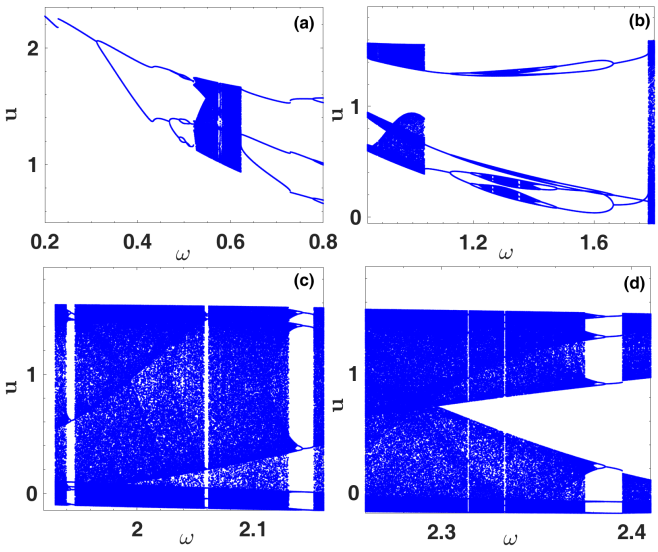


FIG. 19. Enlarged windows of the sTW oscillator bifurcation diagram shown in Figure 18.

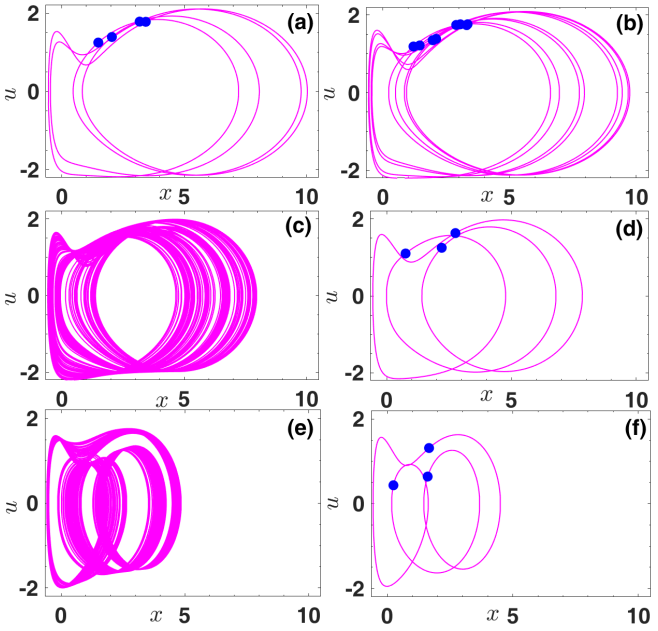


FIG. 20. Phase portraits of the sTW oscillator for selected values of $\omega$ from Fig. 18, illustrating the system's dynamic behavior at: (a) $\omega = 0.485$ (period-4), (b) $\omega = 0.50$ (period-8), (c) $\omega = 0.62$ (chaotic), (d) $\omega = 0.63$ (period-3), (e) $\omega = 1.02$ (chaotic), (f) $\omega = 1.05$ (period-3). The blue dots represent the corresponding points in the Poincaré section

from $\omega \approx 1.943$ to $\omega \approx 1.947$. The transitions shown in the bifurcation diagram are supported by the Lyapunov exponent plot in Fig. 18(b), with stable periodic zones clearly marked by negative Lyapunov exponents, whereas chaotic behaviour is confirmed by positive ones. The phase portraits in Fig. 20(a)–(f) demonstrate that, in contrast to the observed pattern for increasing $f$, the

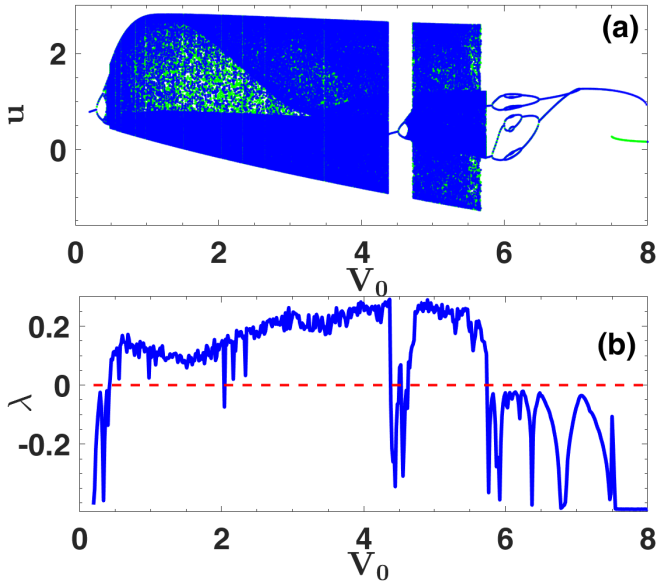


FIG. 21. (a) Bifurcation diagram of the sTW oscillator, illustrating the evolution of the system's behavior with respect to $V_0$. (b) Corresponding maximal Lyapunov exponent as a function of $V_0$, highlighting regions of chaos (positive values) and stability (negative values). Other parameters are fixed at $b_h = 1.0$, $c_h = 0.25$, $r_e = 0$, $\omega = 2.0$, $\delta = 0.8$, $f = 4.0$.

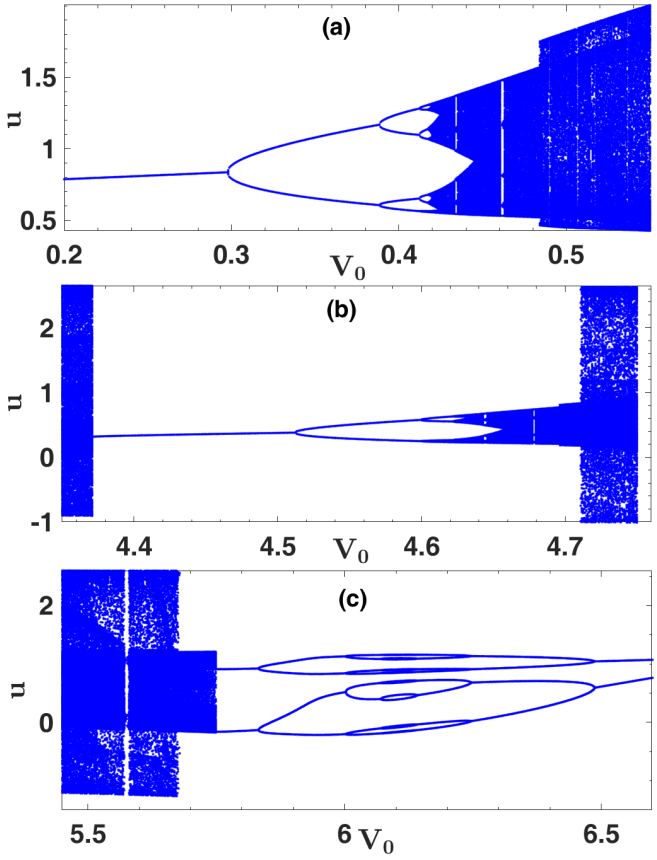


FIG. 22. Enlarged windows of the sTW oscillator bifurcation diagram in Fig. 21.

orbits typically contract as $\omega$ grows.

Now, we proceed to examine the evolution of the system dynamics when the sTW potential parameters change. Fig. 21 presents the bifurcation diagram of the state variable $u$ (panel a) and the corresponding maximal Lyapunov exponent plot in (b) as the dissociation parameter $V_0$ varies from 0 to 8. For detailed views, expanded sections of the bifurcation diagram from Fig. 21(a) are shown in Fig. 22. In addition, the phase portraits depicting the dynamic behavior of the sTW oscillator at different $V_0$ values are provided in Fig. 23. Fig. 22(a) shows that the sTW oscillator exhibits period-1 behavior for lower values of $V_0$ up to roughly $V_0 = 0.3$. It then undergoes a sequence of period-doubling bifurcations before entering a chaotic zone at $V_0 = 0.42$. Notably, a sudden expansion in the size of the chaotic attractor also appears, indicating an interior crisis event at $V_0 = 0.484$. Fig. 23(a) displays the phase portrait just prior to this crisis at $V_0 = 0.483$, and Fig. 23(b) shows the phase portrait following the crisis event at $V_0 = 0.4863$, demonstrating the expansion of the chaotic attractor's domain. A prominent periodic window within the chaotic region of Fig. 21 is expanded in Fig. 22(b). This window shows a period-1 attractor emerging from a boundary crisis at $V_0 \approx 4.371$. The chaotic attractor at $V_0 = 4.37$ just before the boundary crisis is illustrated in Fig. 23(c), and the period-1 attractor that forms at $V_0 = 4.372$ is shown in Fig. 23(d). The period-1 attractor eventually undergoes a period-doubling bifurcation, leading to a narrow-band chaotic attractor (Fig. 23(e)). At $V_0 = 4.711$, an interior crisis causes a notable expansion in the chaotic attractor (Fig. 23(f)), which dominates the dynamics until $V_0 \approx 5.674$, where another interior crisis results in a sudden contraction. Figs. 23(g) and 23(h) shows the phase portraits of the chaotic attractor shortly before and after the crisis at $V_0 = 5.674$. Figure 22(c) shows that the chaotic attractor experiences a boundary crisis at $V_0 \approx 5.75$ due to its collision with a period-2 orbit on its basin boundary. This collision leads to the emergence of a period-2 attractor, followed by period-bubbling characterized by alternating period-doubling and reverse period-doubling transitions stemming from symmetry-breaking. As $V_0$ increases from 5.75 in the course of the period bubbling event, the attractor evolves progressively from period-2 to period-4, then to period-8, and subsequently to period-16 (Fig. 23(i)). As $V_0$ reaches 6.487, the system reverses from period-16 back to period-2 instead of proceeding into chaos, and at $V_0 = 7.05$, it attains stability at a period-1 attractor till $V_0 = 7.5$, when two coexisting period-1 attractors emerge and persists up to $V_0 = 8.0$.

The maximal Lyapunov exponent ($\lambda$) as a function of $V_0$, shown in Fig. 21(b), supports the bifurcation analysis. The chaotic nature in this range is confirmed by the positive values of $\lambda$ up to around $V_0 = 4.5$. Sharp drops to negative $\lambda$ values between $V_0 = 4.5$ and $V_0 = 4.75$

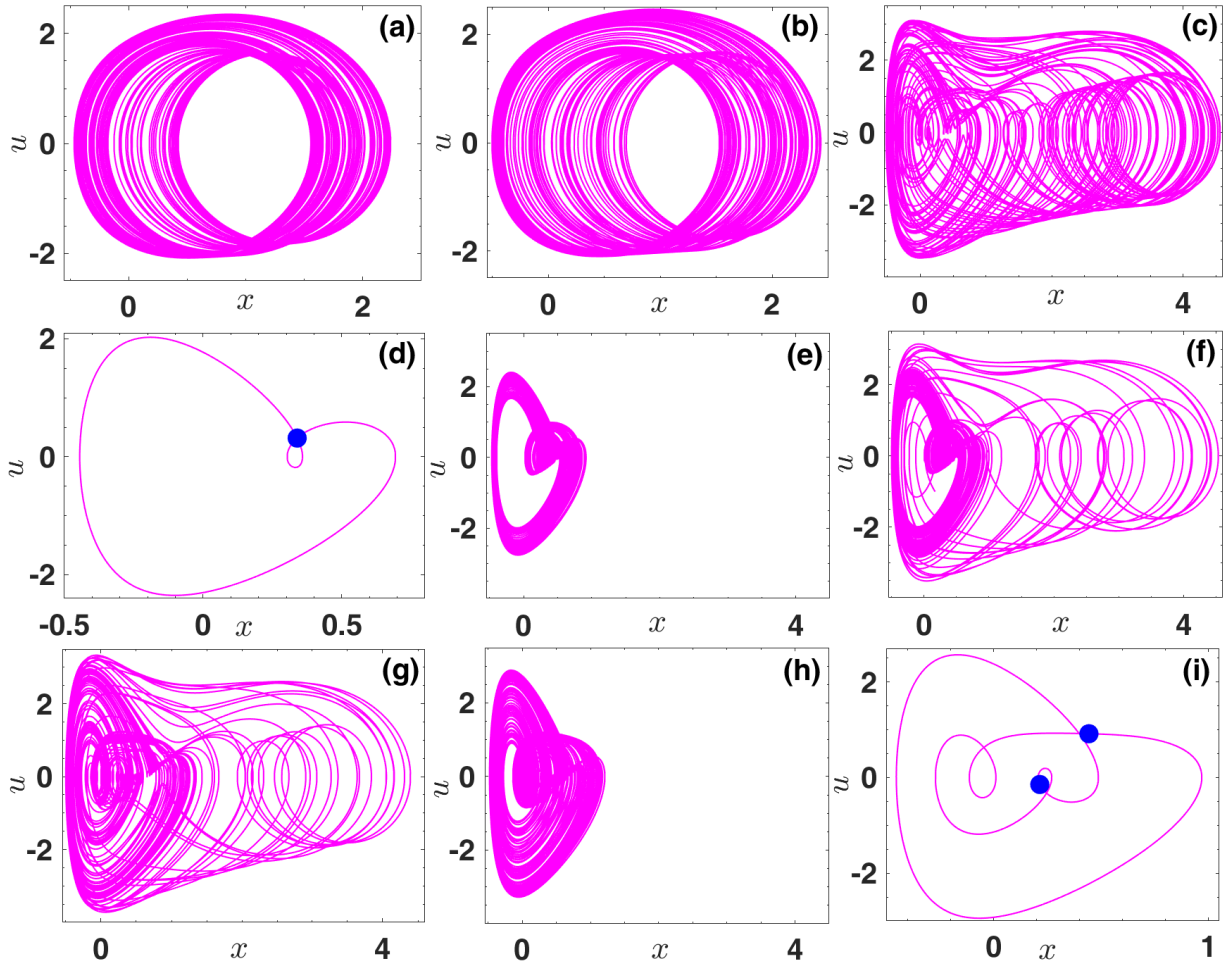


FIG. 23. Phase portraits of the sTW oscillator for selected values of $V_0$ from Fig. 21, illustrating the system's dynamic behaviour at: (a) $V_0 = 0.483$ (chaotic), (b) $V_0 = 0.4863$ (chaotic), (c) $V_0 = 4.37$ (chaotic), (d) $V_0 = 4.372$ (period-1), (e) $V_0 = 4.71$ (chaotic), (f) $V_0 = 4.714$ (chaotic), (g) $V_0 = 5.67$ (chaotic), (h) $V_0 = 5.68$ (chaotic), (i) $V_0 = 5.8$ (period-2). The blue dots represent the corresponding points in the Poincaré section

match the bifurcation diagram's periodic window. The Lyapunov exponent stays positive as $V_0$ rises until around $V_0 = 5.75$, after which it turns negative, indicating stability.

The dynamics of the sTW oscillator as a function of the potential parameter $b_h$ and the corresponding maximal Lyapunov exponent are depicted in Fig. 24. The Lyapunov exponent plot corroborates the bifurcation structure with chaotic regions clearly characterized by positive values and periodic windows by negative values. In Fig. 24(a), it is evident that the oscillator maintains a period-1 oscillation for $b_h$ values up to approximately 0.82, beyond which period-doubling bifurcations initiate a transition to chaos. This chaotic domain occupies a large regime of the $b_h$ parameter space: $b_h = 1.20$ to $b_h = 2.74$. Shown in Fig. 25 are zooms of some $b_h$ regimes capturing clearer pictures of some transitions between chaotic and periodic states. Zoomed-in views in Figs. 25(a) and 25(b) reveal intricate shifts from chaos to periodicity. Within these periodic windows, the periodic orbits are triggered by boundary crises involving chaotic attractors and terminated via sequences of multiple period-doubling bifurcations, forming narrow chaotic bands that merge during attractor merging crises to produce larger chaotic attractors. In Fig. 25(a), we can identify a boundary crisis at $b_h = 1.418$ with the emergence of a period-7 attractor. Phase portraits illustrating the chaotic attractor at $b_h = 1.417$ and the period-7 attractor at $b_h = 1.419$ post-crisis event are shown in Figs. 26(a) and 26(b), respectively. This attractor transitions into narrow chaotic bands (Fig. 26(c)) and undergoes an attractor merging crisis at $b_h \approx 1.427$, with the appearance of the expanded chaotic attractor depicted in Fig. 26(d). A similar boundary crisis at $b_h = 1.43$ yields another period-7 attractor, which subsequently undergoes period-doubling bifurcations, leading to narrow chaotic bands that merge at $b_h = 1.449$. The Poincaré sections depicted in Figs. 27(a) and 27(b) clearly illustrate the attractor-merging crisis event involving the narrow 7-band chaotic attractors.

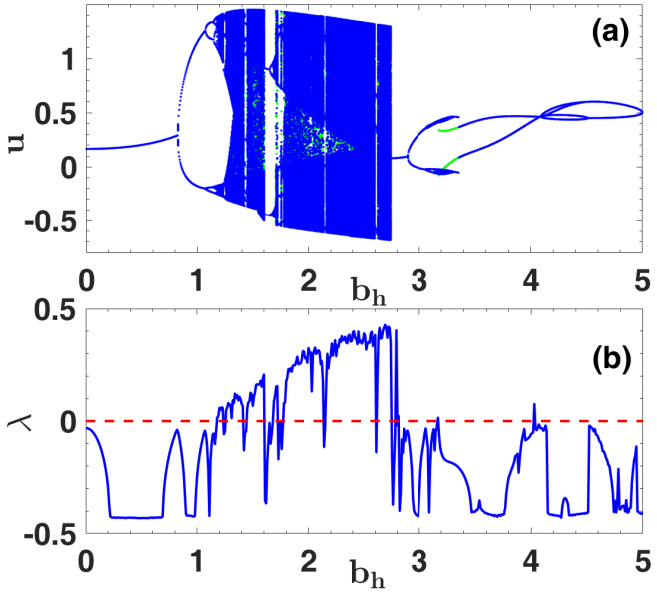


FIG. 24. (a) Bifurcation diagram of the sTW oscillator, illustrating the evolution of the system's behavior with respect to $b_h$. (b) Corresponding maximal Lyapunov exponent, highlighting regions of chaos (positive values) and stability (negative values) as a function of $b_h$. Other parameters are fixed at $c_h = 0.25$, $r_e = 0$, $V_0 = 1.0$, $\omega = 3.0$, $\delta = 0.8$, $f = 2.0$.

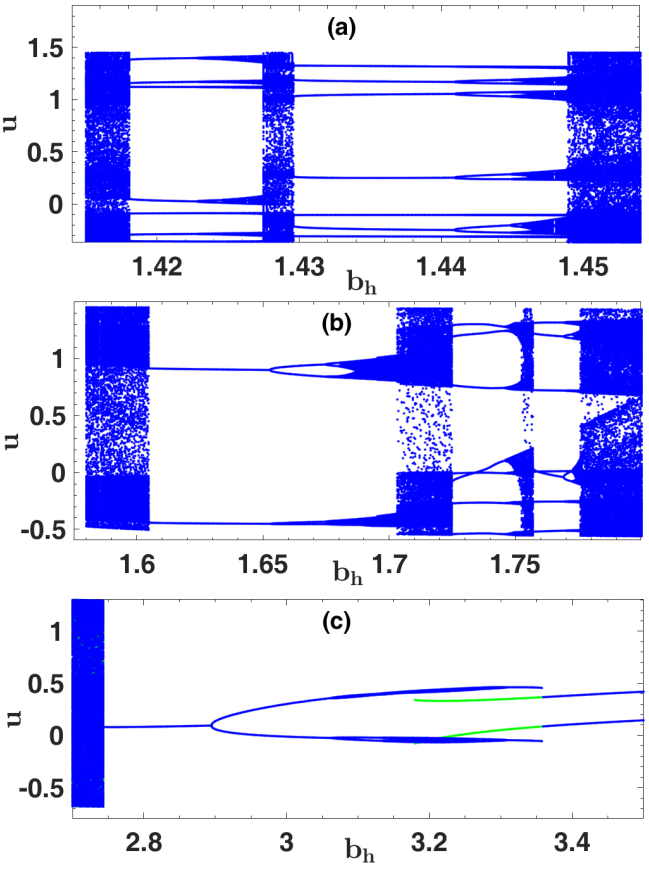


FIG. 25. Enlarged windows of the sTW oscillator bifurcation diagram in Fig. 24.

Figure 25(b) highlights a boundary crisis event at $b_h = 1.605$ from which a period-2 attractor is born and its subsequent period-doubling route to narrow chaotic bands. As $b_h$ takes on higher values, these bands merge into a larger chaotic orbits in an attractor-merging crisis event at $b_h \approx 1.703$. The phase portrait at $b_h = 1.60$ just before the boundary crisis is shown in Fig. 26(e), while Fig. 26(f) presents the period-2 attractor at $b_h = 1.61$ post-crisis. The phase portrait and corresponding Poincaré section illustrating the two narrow chaotic bands at $b_h = 1.70$ are depicted in Figs. 26(g) and 27(c), respectively. Similarly, Figs. 26(h) and 27(d) show the phase portrait and Poincaré section of the merged attractor at $b_h = 1.71$. Other regions with period-7 attractors are noted between $1.725 < b_h < 1.746$ and $1.757 < b_h < 1.769$. For higher values of $b_h$, the dynamics is dominated by periodic orbits. Figure 25(c) indicates a period-1 attractor emerging from a boundary crisis at $b_h = 2.743$. Beyond $b_h = 2.9$, the oscillator predominantly exhibits period-1 or period-2 orbits, with the appearance of multistability for $3.18 < b_h < 3.36$. Here, a period-2 attractor coexists with a quasi-periodic orbit. The corresponding basins of attraction for the two states are shown in Fig. 28. The basin of attraction in Fig. 28 appears to have a fractal boundary, where the different attractor regions (blue and green) are interwoven in a highly irregular and intricate pattern. This fractal structure indicates a sensitive dependence on initial conditions, where even minute changes in the starting values can cause the system to end up on a different attractor.

The bifurcation diagram, shown in Fig. 29, illustrates how the sTW oscillator dynamically changes as the optimisation parameter $c_h$ changes while maintaining the other parameters at $b_h = 1.0$, $V_0 = 4.0$, $\omega = 0.75$, $\delta = 0.8$, and $f = 2.5$. As $c_h$ spans the interval $-0.2 \leq c_h \leq 0.2$, Fig. 29(a) shows that negative $c_h$ values favour the occurrence of chaotic solutions coexisting with periodic states, while positive $c_h$ values stabilize the system to periodic states. According to the table of spectroscopic parameters (Table I), all the molecules investigated, namely, CO, $O_2$, $I_2$, $H_2$, $Cl_2$ and HF, will potentially exhibit periodic oscillations with their $c_h$ values lying in the range $0 < c_h < 0.2$. However, the dynamics can be complicated and, indeed, extremely unpredictable with the coexistence of three different attractors over the positive $c_h$ parameter values, suggesting that, depending on the chosen initial conditions, the system may settle onto one of three possible final states. This complexity due to initial state sensitivity carries significant implications for experimental applications. The dynamics is even more complex for negative $c_h$ parameter values, with chaotic and periodic states coexisting in the neighborhood of $c_h = -0.12$ and $c_h = -0.02$. We mapped out which initial conditions $(x_0, u_0)$ converge to specific attractors, by examining the basins of attraction at $c_h = -0.04$. Figure 30 depicts the basins of attraction for $c_h = -0.04$. It provides details on how different initial conditions $(x_0, u_0)$ direct the system to particular attractors. The color-coding in the

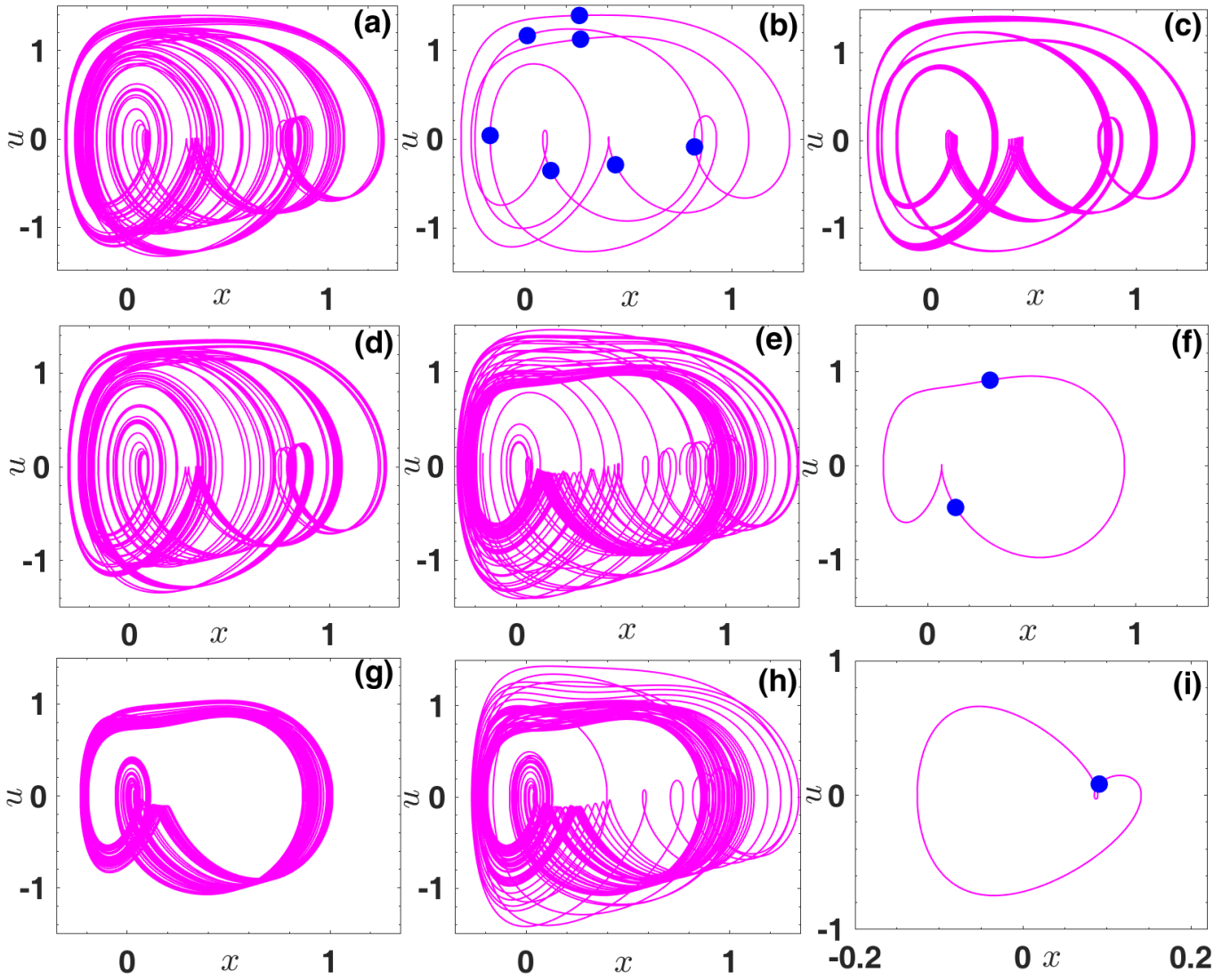


FIG. 26. Phase portraits of the sTW oscillator for selected values of $b_h$ from Fig. 24, illustrating the system's dynamic behaviour at: (a) $b_h = 1.417$ (chaotic), (b) $b_h = 1.419$ (period-7), (c) $b_h = 1.427$ (chaotic), (d) $b_h = 1.428$ (chaotic), (e) $b_h = 1.60$ (chaotic), (f) $b_h = 1.61$ (period-2), (g) $b_h = 1.70$ (chaotic), (h) $b_h = 1.71$ (chaotic), (i) $b_h = 2.8$ (period-1). The blue dots represent the corresponding points in the Poincaré section.

figure distinguishes the attractors: white regions represent a coexisting period-2 attractor, blue areas denote a period-2 attractor, and green indicates chaotic attractors. The basin is characterized by a fractal-like, intricate structure with intertwined regions that suggest a complex boundary between basins. Such a structure, known as a Wada basin [104–106] and first observed by Nusse *et al.* [104], is characterised by boundaries that connect two other basins. The basin features are indicative of the system's extremely sensitive dependence on initial conditions, where minor changes in the starting point can yield significantly different outcomes.

Finally, Figure 31 provides phase portraits for $c_h = -0.04$, showing the coexistence of various attractors for slightly different initial conditions. In Fig. 31(a), a period-2 attractor is shown for initial conditions $(x_0, u_0) = (4.85, 4.5)$, where the trajectory forms a stable, repeating loop. Fig. 31(b) depicts another period-2 attractor for slightly different initial conditions $(x_0, u_0) = (4.85, 4.7)$, with a similar but distinct configuration from Fig. 31(a). Both portraits correspond to basins associated with periodic solutions, as depicted in Fig. 30. Figure 31(c) depicts a chaotic attractor for initial conditions $(x_0, u_0) = (4.85, 4.3)$. Unlike the periodic cases, this chaotic attractor follows a non-repeating, complex path characteristic of chaotic dynamics. This behavior aligns with the chaotic basin shown with green color in Fig. 30. Fig. 31(d) displays a Poincaré section of the chaotic attractor shown in Fig. 31(c), revealing its intricate, fractal-like nature and emphasizing the system's complex behavior. This figure reinforces the notion of sensitivity to initial conditions, where slight changes can shift the system

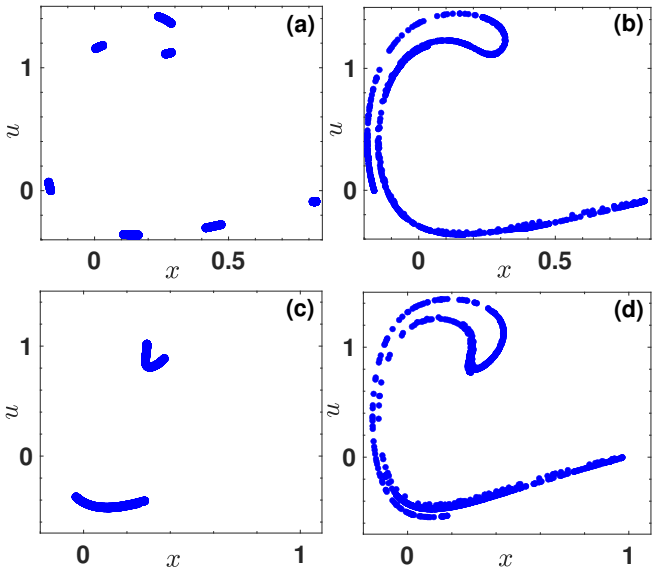


FIG. 27. Poincaré section of the sTW oscillator illustrating the attractor-merging crises shown in Figs. 26(c), (d), (g) and (h): (a) $b_h = 1.427$ (narrow 7-band chaotic attractor just before crisis), (b) $b_h = 1.428$ (chaotic attractor just after crisis), (c) $b_h = 1.70$ (narrow 2-band chaotic attractor just before crisis), (d) $b_h = 1.71$ (chaotic attractor just after crisis).

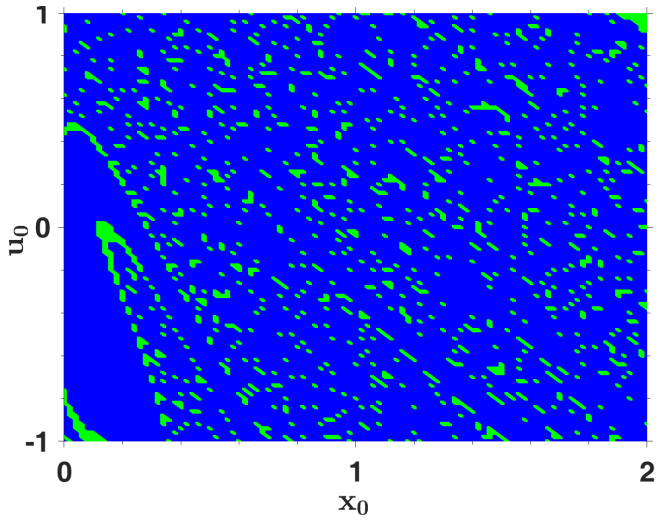


FIG. 28. Basins of attraction of the coexisting attractors in Fig. 25(c) for $b_h = 3.25$ (coexisting period-2 (blue) and quasi-periodic attractor (green)).

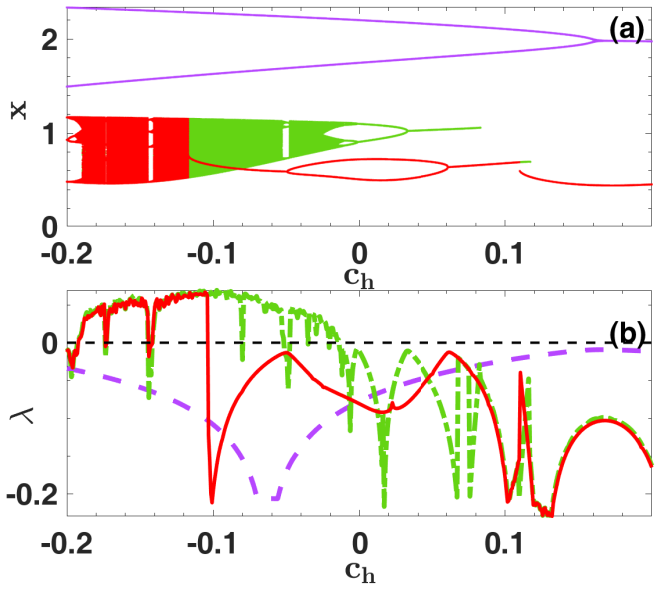


FIG. 29. (a) Bifurcation diagram of the sTW oscillator, illustrating the evolution of the system's behavior with respect to $c_h$. (b) Corresponding maximal Lyapunov exponent: Green dash-dot line (green bifurcation branch), red solid-line (red bifurcation branch), and purple dash-line (purple bifurcation branch)), highlighting regions of chaos (positive values) and stability (negative values). Other parameters are fixed at $b_h = 1.0$, $r_e = 0$, $V_0 = 4.0$, $\omega = 0.75$, $\delta = 0.8$, $f = 2.5$.

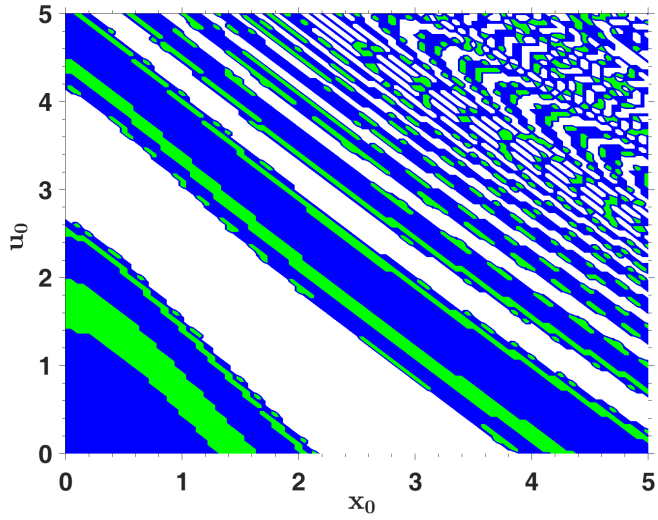


FIG. 30. Basins of attraction of the coexisting attractors in Fig. 29 for $c_h = -0.04$ (coexisting period-2 (white), period-2 (blue) and chaotic attractors (green))

from periodic to chaotic attractors, typical of the Wada basin's shared boundary feature. Fig. 29(b) depicts the maximal Lyapunov exponent $\lambda$ as a function of $c_h$, which provides quantitative insight into the attractors' stability. The black curve represents $\lambda$ for the chaotic (blue) attractor, while the green curve corresponds to the red attractor. Positive $\lambda$ values indicate chaotic behavior, whereas negative values denote stability. For $c_h < 0.1$, the black curve predominantly shows positive $\lambda$, confirming chaotic behavior, but it transitions to negative values near $c_h = 0.1$, marking a shift toward stability. This trend in $\lambda$ aligns with the observed transitions in the behavior of the red attractor.

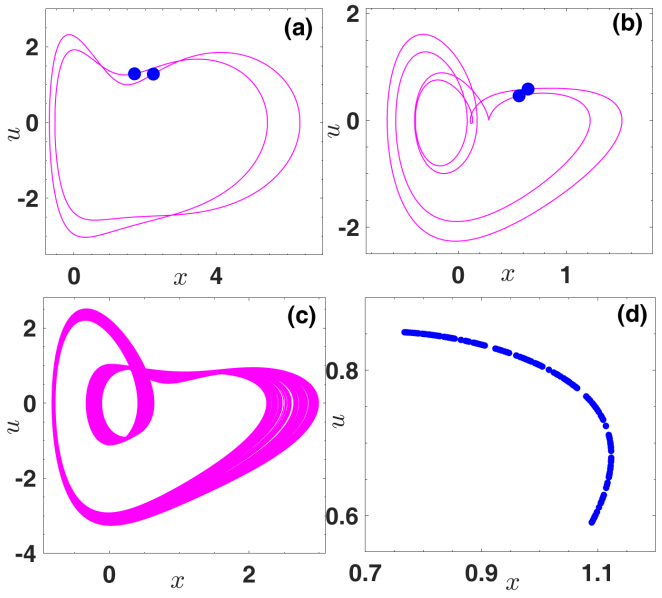


FIG. 31. Phase portraits of the sTW oscillator for $c_h = -0.04$ for three very close initial conditions $(x_0, u_0)$ : (a) $(x_0, u_0) = (4.85, 4.5)$ (period-2 attractor for the orange branch in Fig. 29(a)), (b) $(x_0, u_0) = (4.85, 4.7)$ (period-2 attractor for the blue branch in Fig. 29(a)); and (c) $(x_0, u_0) = (4.85, 4.3)$ (chaotic attractor for the green branch in Fig. 29(a)). (d) is the Poincaré section of the phase portrait in (c). The blue dots represent the corresponding points in the Poincaré section.

## V. CONCLUDING REMARKS

In this paper, we have analysed the resonance and bifurcation characteristics of the driven shifted Tietz-Wei (sTW) oscillator for six diatomic molecules, focusing on the interplay between the external driving force and spectroscopic parameters, namely, the amplitude ($f$), frequency ($\omega$), dissociation energy ($V_0$), and potential optimization parameters ($b_h$ and $c_h$).

We have explored the primary and superharmonic resonances using the response equation obtained analytically by means of multiple time scales method. We found that less rigidly bonded molecules are more responsive to external excitations, with $I_2$ and $Cl_2$ molecules exhibiting the highest-amplitude responses in primary resonance due to their lower dissociation energies. Despite being the lightest of the molecules studied, $H_2$ exhibited a significant high amplitude response, whereas CO and $O_2$, with their higher $V_0$ values, showed lower responses. Variations in $F_0$, $b_h$, and $c_h$ substantially impacted the primary resonance behavior. Higher $F_0$ and lower $V_0$ values increased the response amplitude and expanded the hysteresis frequency range. Variations in $b_h$ and $c_h$, in general, altered the peak values and the hysteresis frequency range of primary resonance, with less visible impact on superharmonic resonances. Furthermore, the superharmonic resonance showed increased amplitudes and considerable hysteresis, especially for $I_2$ and $Cl_2$, with lower $V_0$ and greater $F_0$ magnifying the nonlinear response.

Bifurcation diagrams and the corresponding maximal Lyapunov exponents were explored by varying the relevant parameters. The attractor landscape underwent period-doubling routes to chaos and sudden chaotic transitions, interspersed with periodic windows and crisis events including boundary crises, interior crises, and attractor-merging crises. At different parameter levels, saddle-node bifurcations, symmetry-breaking, attractor bubbling, and multistability were found. Multistability was explored through the basins of attraction and phase portraits corresponding to closely-situated initial conditions. Striped basins indicating the coexistence of periodic and chaotic states, fractal basins with intricately interwoven attractor regions, and Wada basins with three coexisting attractors, were found. The results underscore the rich and complex dynamics attributable to the sensitive dependence on initial conditions – and highlighting the challenges in predicting the long-term behavior of diatomic molecules. This work contributes to the broader field of nonlinear dynamics and, in particular, to molecular physics by demonstrating the complexity that arises from interactions between the spectroscopic properties of multi-parameter diatomic molecular systems and the external driving force.

The results carry significant implications for experimental applications. For example, the $Cl_2$ molecule, which demonstrated the highest-amplitude responses in primary resonance in this study, exhibits pronounced anisotropy in its potential energy landscape, as reported by Selmi *et al.* [107] – implying that the energy landscape changes with the molecular geometry and potentially giving rise to multiple stable or metastable electronic states [107]. This kind of behavior is associated with multistability [26, 107]. The presence of multiple excited states and their interactions, especially through nonadiabatic transitions, opens up diverse photodissociation pathways – a hallmark of systems with multistable electronic configurations [107]. Indeed, there is compelling experimental evidence that $Cl_2$ has multiple excited electronic states. A particularly illuminating work by Zhang *et al.* [108], on the multi-electron ionization and dissociation of $Cl_2$ in a near-infrared femtosecond laser field, revealed that the singly-charged molecular ion $Cl_2^+$ dissociates from two distinct excited states: $X^2\Pi_u$ and $X^2\sum g^+$, linked to ionization from the HOMO-1 and HOMO-2 orbitals, respectively. By exploring higher charge states ($Cl_2^{n+}$, $n = 2-8$), Zhang *et al.* [108] further confirmed the existence of the multiple excited states that play critical roles in the photodissociation dynamics of $Cl_2$.

Similarly, the $O_2$ molecule exhibits a rich electronic structure, with strong experimental evidence for complex multiple excited states, namely, a singlet delta state ($X^1\Delta g$) [109, 110], a singlet sigma state ($X^1\sum g$) [110, 111], a triplet ground state ($X^3\sum^- g$) [110, 111], and other metastable states such as $O_2(a^1\Delta g)$ and

$O_2(b^1\sum g^+)$ [111], all of which play crucial roles in atmospheric chemistry and photophysics, as well as in plasma processes. Finally, it is worth mentioning that both iodine ($I_2$) and carbon monoxide (CO), investigated above, exhibit multiple excited electronic states whose existence is well-supported by both theoretical and experimental studies [112–115].

## ACKNOWLEDGMENTS

We acknowledge the support of the Engineering and Physical Sciences Research Council (United Kingdom) under Grant No. EP/X004597/1.

## DATA AVAILABILITY

There are no additional data, beyond those that are already presented herein, to support the findings of this theoretical article.


[1] U. E. Vincent and O. Kolebaje, Introduction to the dynamics of driven nonlinear systems, Contemp. Phys. **61**, 169 (2020).

[2] J. L. Mateos, Chaotic transport and current reversal in deterministic ratchets, Phys. Rev. Lett. **84**, 258 (2000).

[3] E. Ott, *Chaos in Dynamical Systems* (Cambridge University Press, Cambridge, 2002).

[4] U. E. Vincent, A. Kenfack, A. N. Njah, and O. Akinlade, Bifurcation and chaos in coupled ratchets exhibiting synchronized dynamics, Phys. Rev. E **72**, 056213 (2005).

[5] G. C. Layek and N. C. Pati, Bifurcations and chaos in convection taking non-Fourier heat-flux, Phys. Lett. A **381**, 3568 (2017).

[6] G. C. Layek and N. C. Pati, Bifurcations and hyperchaos in magnetoconvection of non-Newtonian fluids, Int. J. Bifurc. Chaos **28**, 1830034 (2018).

[7] J. Li, H. Gu, Y. Jiang, and Y. Li, Different bifurcations and slow dynamics underlying different stochastic dynamics of slow, medium, and fast bursting of $\beta$-cell, Nonlinear Dyn. **112**, 20309 (2024).

[8] S. P. Dawson, C. Grebogi, J. A. Yorke, I. Kan, and H. Koçak, Antimonotonicity: inevitable reversals of period-doubling cascades, Phys. Lett. A **162**, 249 (1992).

[9] I. Sami Doubla, B. Ramakrishnan, Z. Tabekoueng Njitacke, J. Kengne, and K. Rajagopal, Hidden extreme multistability and its control with selection of a desired attractor in a non-autonomous Hopfield neuron, AEU - Int. J. Elec. Comm. **144**, 154059 (2022).

[10] X. Han, Q. Bi, P. Ji, and J. Kurths, Fast-slow analysis for parametrically and externally excited systems with two slow rationally related excitation frequencies, Phys. Rev. E **92**, 012911 (2015).

[11] N. M. Awal and I. R. Epstein, Period-doubling route to mixed-mode chaos, Phys. Rev. E **104**, 024211 (2021).

[12] K. S. Oyeleke, O. I. Olusola, O. T. Kolebaje, U. E. Vincent, A. B. Adeloye, and P. V. E. McClintock, Novel bursting oscillations in a nonlinear gyroscope oscillator, Phys. Scr. **97**, 085211 (2022).

[13] W. Lyu, S. Li, J. Huang, and Q. Bi, Occurrence of mixed-mode oscillations in a system consisting of a Van der Pol system and a Duffing oscillator with two potential wells, Nonlinear Dyn. **112**, 5997 (2024).

[14] S. Rajasekar and M. A. F. Sanjuan, *Nonlinear Resonances*, 1st ed. (Springer Series in Synergetics, Switzerland, 2016).

[15] I. Kovacic, *Nonlinear Oscillations: Exact Solutions and their Approximations* (Springer Nature, Switzerland, 2020).

[16] E. Ryd and H. Kantz, Nonlinear resonance in an overdamped Duffing oscillator as a model of paleoclimate oscillations, Phys. Rev. E **110**, 034213 (2024).

[17] P. O. Adesina, U. E. Vincent, T. O. Roy-Layinde, O. T. Kolebaje, and P. V. E. McClintock, Crisis-induced vibrational resonance in a phase-modulated periodic structure, Phys. Rev. E **110**, 034215 (2024).

[18] A. Pikovsky, M. Rosenblum, and J. Kurths, *Synchronization: A Universal Concept in Nonlinear Sciences* (Cambridge University Press, Cambridge, 2000).

[19] U. E. Vincent, A. Kenfack, D. V. Senthilkumar, D. Mayer, and J. Kurths, Current reversals and synchronization in coupled ratchets, Phys. Rev. E **82**, 046208 (2010).

[20] U. E. Vincent, B. R. Nana-Nbendjo, and P. V. E. McClintock, Collective dynamics of a network of ratchets coupled via a stochastic dynamical environment, Phys. Rev. E **87**, 022913 (2013).

[21] D. Butusov, V. Rybin, and A. Karimov, Fast time-reversible synchronization of chaotic systems, Phys. Rev. E **111**, 014213 (2025).

[22] J. G. Freire, C. Bonatto, C. C. DaCamara, and J. A. C. Gallas, Multistability, phase diagrams, and intransitivity in the Lorenz-84 low-order atmospheric circulation model, Chaos **18** (2008).

[23] A. Chudzik, P. Perlikowski, A. Stefanski, and T. Kapitaniak, Multistability and rare attractors in van der Pol–Duffing oscillator, Int. J. Bifurc. Chaos **21**, 1907 (2011).

[24] L. Ying, D. Huang, and Y.-C. Lai, Multistability, chaos, and random signal generation in semiconductor superlattices, Phys. Rev. E **93**, 062204 (2016).

[25] J.-f. Shi, X.-f. Gou, and L.-y. Zhu, Bifurcation of multistable behaviors in a two-parameter plane for a non-smooth nonlinear system with time-varying parameters, Nonlinear Dyn. **100**, 3347 (2020).

[26] A. N. Pisarchik and U. Feudel, Control of multistability, Phys. Rep. **540**, 167 (2014).

[27] A. N. Pisarchik and A. E. Hramov, *Multistability in Physical and Living Systems* (Springer, Cham, Switzerland, 2022).

[28] C. N. Ngonghala, U. Feudel, and K. Showalter, Extreme multistability in a chemical model system, Phys. Rev. E **83**, 056206 (2011).

[29] A. N. Pisarchik, R. Jaimes-Reátegui, C. Rodríguez-Flores, J. García-López, G. Huerta-Cuéllar, and F. J. Martín-Pasquín, Secure chaotic communication based on extreme multistability, J. Franklin Inst. **358**, 2561 (2021).

[30] S. Kumarasamy, S. Leo Kingston, S. Srinivasan, A. Chudzik, T. Kathamuthu, and T. Kapitaniak, Extreme events and extreme multistability in a nearly conservative system, Chaos **34** (2024).

[31] J. C. Sprott, S. Jafari, A. J. M. Khalaf, and T. Kapitaniak, Megastability: Coexistence of a countable infinity of nested attractors in a periodically-forced oscillator with spatially-periodic damping, Eur. Phys. J. ST. **226**, 1979 (2017).

[32] P. Prakash, K. Rajagopal, J. P. Singh, and B. K. Roy, Megastability, multistability in a periodically forced conservative and dissipative system with signum nonlinearity, Int. J. Bifurc. Chaos **28**, 1830030 (2018).

[33] P. Prakash, K. Rajagopal, J. P. Singh, and B. K. Roy, Megastability in a quasi-periodically forced system exhibiting multistability, quasi-periodic behaviour, and its analogue circuit simulation, AEU-Int. J. Electron. Commun. **92**, 111 (2018).

[34] A. Karimov, I. Babkin, V. Rybin, and D. Butusov, Matryoshka multistability: Coexistence of an infinite number of exactly self-similar nested attractors in a fractal phase space, Chaos, Sol. & Fract. **187**, 115412 (2024).

[35] S. Kumarasamy, M. Banerjee, V. Varshney, M. D. Shrimali, N. V. Kuznetsov, and A. Prasad, Saddle-node bifurcation of periodic orbit route to hidden attractors, Phys. Rev. E **107**, L052201 (2023).

[36] I. R. Garashchuk, A. O. Kazakov, and D. I. Sinelshchikov, Synchronous oscillations and symmetry breaking in a model of two interacting ultrasound contrast agents, Nonlinear Dyn. **101**, 1199 (2020).

[37] M. Golos, V. Jirsa, and E. Daucé, Multistability in large scale models of brain activity, PLoS Comp. Bio. **11**, e1004644 (2015).

[38] D. Jaeger and R. Jung, *Encyclopedia of Computational Neuroscience* (Springer, New York, 2022).

[39] J. Kengne, Z. Njitacke Tabekoueng, and H. Fotsin, Coexistence of multiple attractors and crisis route to chaos in autonomous third order Duffing–Holmes type chaotic oscillators, Commun. Nonlin. Sci. Numer. **36**, 29 (2016).

[40] N. Wang, G. Zhang, and H. Bao, Bursting oscillations and coexisting attractors in a simple memristor-capacitor-based chaotic circuit, Nonlinear Dyn. **97**, 1477 (2019).

[41] A. K. Farhan, R. S. Ali, H. Natiq, and N. M. Al-Saidi, A new S-box generation algorithm based on multistability behavior of a plasma perturbation model, IEEE Access **7**, 124914 (2019).

[42] T. Bonny, S. Vaidyanathan, A. Sambas, K. Benkouider, W. Al Nassan, and O. Naqaweh, Multistability and bifurcation analysis of a novel 3D jerk system: Electronic circuit design, FPGA implementation, and image cryptography scheme, IEEE Access **11**, 78584 (2023).

[43] K. Benkouider, A. Sambas, T. Bonny, W. Al Nassan, I. A. Moghrabi, I. M. Sulaiman, B. A. Hassan, and M. Mamat, A comprehensive study of the novel 4D hyperchaotic system with self-exited multistability and application in the voice encryption, Sci. Rep. **14**, 12993 (2024).

[44] N. Kacem and S. Hentz, Bifurcation topology tuning of a mixed behavior in nonlinear micromechanical resonators, Appl. Phys. Lett. **95** (2009).

[45] P. V. Savi and M. A. Savi, Nonlinear dynamics of an adaptive energy harvester with magnetic interactions and magnetostrictive transduction, Smart Struct. & Syst. **33**, 281 (2024).

[46] L. G. Costa, L. L. Monteiro, and M. A. Savi, Multistability investigation for improved performance in a compact nonlinear energy harvester, J. Braz. Soc. Mech. Sci. & Eng. **46**, 212 (2024).

[47] A. L. Kawczyński and B. Nowakowski, Stochastic transitions through unstable limit cycles in a model of bistable thermochemical system, Phys. Chem. Chem. Phys. **10**, 289 (2008).

[48] S. T. Tanekou, J. Ramadoss, J. Kengne, G. D. Kenmoe, and K. Rajagopal, Coexistence of periodic, chaotic and hyperchaotic attractors in a system consisting of a Duffing oscillator coupled to a Van der Pol oscillator, Int. J. Bifurc. Chaos **33**, 2330004 (2023).

[49] J. Venkatesh, J. Ramadoss, J. C. Chedjou, K. Jacques, and K. Rajagopal, On the occurrence of multiscroll and multistable dynamics in a star network of four nonlinearly coupled self-driven Duffing–Rayleigh oscillators, Eur. Phys. J. ST , 1 (2024).

[50] J. H. T. Mbé, M. C. Njidjou, A. F. Talla, P. Woafo, and Y. K. Chembo, Multistability, relaxation oscillations, and chaos in time-delayed optoelectronic oscillators with direct laser modulation, Opt. Lett. **49**, 1277 (2024).

[51] Y. Xiong, Y. Shi, J. Chen, Z. T. Njitacke, D. Jiang, and J. Wu, Multistability and its control in a Van der Pol oscillator coupled with Duffing oscillator through the velocity, Mod. Phys. Lett. B **00**, 2550077 (2025).

[52] Z. G. Nicolaou, S. B. Nicholson, A. E. Motter, and J. R. Green, Prevalence of multistability and nonstationarity in driven chemical networks, J. Chem. Phys. **158** (2023).

[53] Y. J. F. Kpomahou, A. J. Adéchinan, J. K. Agbélélé, and C. Adéyèmi, Parametric vibrational resonance and multistability in biharmonically driven Briggs-Rauscher chemical system, Chin. J. Phys. https://doi.org/10.1016/j.cjph.2024.12.015 (2024).

[54] A. Abdikian, J. Tamang, and A. Saha, Supernonlinear wave and multistability in magneto-rotating plasma with (r, q) distributed electrons, Phys. Scr. **96**, 095605 (2021).

[55] A. A. C. Recco, J. C. Sagás, and P. C. Rech, Multistability, period-adding, and fractality in a plasma oscillator, Phys. Plasmas **30**, 112301 (2023).

[56] S. Fatima, N. Abbas, and M. Munawar, Dynamical profile and multi-stability of ion-acoustic waves with soliton solution arising in plasma physics, Int. J. Geom. Meth. Mod. Phys. **20**, 2350240 (2023).

[57] S. Qiao and C. Gao, Complex dynamics of a non-smooth temperature-sensitive memristive wilson neuron model, Commun. Nonlin. Sci. Numer. **125**, 107410 (2023).

[58] P. Miao, D. Li, and Y. Yue, Two-parameter dynamics and multistability of a non-smooth railway wheelset system with dry friction damping, Chaos **34**, 113118

(2024).
[59] E. Buks, Disentanglement-induced multistability, Phys. Rev. A **110**, 012439 (2024).
[60] Zhu, Ronghui and del Rio-Salgado, Jesus M. and Garcia-Ojalvo, Jordi and Elowitz, Michael B., Synthetic multistability in mammalian cells, Science **375**, eabg9765 (2022).
[61] D. Dudkowski, K. Czołczyński, and T. Kapitaniak, Multistability and synchronization: The co-existence of synchronous patterns in coupled pendula, Mech. Sys. & Signal Proc. **166**, 108446 (2022).
[62] A. Keşkekler, V. Bos, A. M. Aragón, P. G. Steeneken, and F. Alijani, Multimode nonlinear dynamics of graphene resonators, Phys. Rev. Appl. **20**, 064020 (2023).
[63] M.-X. Bi, H. Fan, X.-H. Yan, and Y.-C. Lai, Folding state within a hysteresis loop: Hidden multistability in nonlinear physical systems, Phys. Rev. Lett. **132**, 137201 (2024).
[64] R. Kumar, M. K. Singh, S. Mahajan, and A. B. Bhattacherjee, Study of optical bistability/multistability and transparency in cavity-assisted-hybrid optomechanical system embedded with quantum dot molecules, Opt & Quantum Elec. **56**, 91 (2024).
[65] S. Mahajan, N. Aggarwal, and A. B. Bhattacherjee, Tunable multistability, optomechanically induced transparency and fast-to-slow light transitions in a quadratically coupled electro-optomechanical system consisting of Kerr medium, Opt. & Quantum Elec. **57**, 1 (2025).
[66] B. J. Falaye, S. M. Ikhdair, and M. Hamzavi, Shifted Tietz–Wei oscillator for simulating the atomic interaction in diatomic molecules, J. Theor. Appl. Phys. **9**, 151–158 (2015).
[67] K. P. Huber and G. Herzberg, *Molecular spectra and molecular structure: IV. Constants of diatomic molecules* (Springer Science & Business Media, New York, 2013).
[68] W. Li, Z. Liu, Z. Wang, and H. Dou, Experimental and theoretical analysis of effects of atomic, diatomic and polyatomic inert gases in air and EGR on mixture properties, combustion, thermal efficiency and NOx emissions of a pilot-ignited NG engine, Energy Convers. Manag. **105**, 1082 (2015).
[69] C. G. Parigger and J. O. Hornkohl, *Quantum Mechanics of the Diatomic Molecule with Applications* (IOP Publishing, London, 2019).
[70] X. Liu, S. Truppe, G. Meijer, and J. Pérez-Ríos, The diatomic molecular spectroscopy database, J. Cheminform. **12**, 1 (2020).
[71] C. G. Parigger, Fundamentals of diatomic molecular spectroscopy, Foundations **1**, 208 (2021).
[72] P. S. Barklem and R. Collet, Partition functions and equilibrium constants for diatomic molecules and atoms of astrophysical interest, A&A **588**, A96 (2016).
[73] L. K. McKemmish, Molecular diatomic spectroscopy data, Wiley Interdiscip. Rev. Comput. Mol. Sci. **11**, e1520 (2021).
[74] Z. P. Izgi, The solutions of diatomic models arising in material science, Pramana **96**, 159 (2022).
[75] V. V. Flambaum and V. A. Dzuba, Electric dipole moments of atoms and molecules produced by enhanced nuclear Schiff moments, Phys. Rev. A **101**, 042504 (2020).
[76] M. Abu-Shady and E. M. Khokha, On prediction of the fractional vibrational energies for diatomic molecules with the improved Tietz potential, Mol. Phys. **120**, e2140720 (2022).
[77] O. G. Abamba, O. T. Kolebaje, U. E. Vincent, and P. V. E. McClintock, Vibrational resonance in bichromatically excited diatomic molecules in a shifted molecular potential, Phys. Rev. E **110**, 034209 (2024).
[78] M. S. Abdelmonem, A. Abdel-Hady, and I. Nasser, Dealing with the shifted and inverted Tietz–Hua oscillator potential using the J-matrix method, Int. J. Quantum Chem. **116**, 897 (2016).
[79] U. S. Okorie, E. E. Ibekwe, M. C. Onyeaju, and A. N. Ikot, Solutions of the Dirac and Schrödinger equations with shifted Tietz-Wei potential, Eur. Phys. J. Plus **133**, 1 (2018).
[80] C. A. Onate, M. C. Onyeaju, E. E. Ituen, A. N. Ikot, O. Ebomwonyi, J. O. Okoro, and K. O. Dopamu, Eigensolutions, Shannon entropy and information energy for modified Tietz-Hua potential, Indian J. Phys. **92**, 487 (2018).
[81] A. N. Ikot, W. Azogor, U. S. Okorie, F. E. Bazuaye, M. C. Onjeaju, C. A. Onate, and E. O. Chukwuocha, Exact and Poisson summation thermodynamic properties for diatomic molecules with shifted Tietz potential, Indian J. Phys. **93**, 1171 (2019).
[82] R. Horchani and H. Jelassi, Comments on the paper "Exact and Poisson summation thermodynamic properties for diatomic molecules with shifted Tietz potential", Indian J. Phys. **96**, 373 (2022).
[83] U. S. Okorie, A. N. Ikot, G. J. Rampho, M. C. Onyeaju, M. U. Ibezim-Ezeani, and A. Abdel-Aty, Bound and scattering states of the Klein-Gordon equation for shifted Tietz-Wei potential with applications to diatomic molecules, Mol. Phys. **119**, 1171 (2021).
[84] R. Horchani, S. Shafii, H. Friha, and H. Jelassi, A straightforward model for molar enthalpy prediction of CsO, CsF, and CsCl molecules via shifted Tietz-Wei potential, Int. J. Thermophys. **42**, 84 (2021).
[85] R. Horchani and H. Jelassi, A four-parameters model for molar entropy calculation of diatomic molecules via shifted Tietz-Wei potential, Chem. Phys. Lett. **753**, 137583 (2020).
[86] W. Knop and W. Lauterborn, Bifurcation structure of the classical Morse oscillator, J. Chem. Phys. **93**, 3950 (1990).
[87] Z. Jing, J. Deng, and J. Yang, Bifurcations of periodic orbits and chaos in damped and driven Morse oscillator, Chaos Soliton Fract. **35**, 486 (2008).
[88] K. Abirami, S. Rajasekar, and M. A. F. Sanjuán, Vibrational resonance in the Morse oscillator, Pramana **81**, 127 (2013).
[89] A. K. de Almeida Jr., R. Egydio de Carvalho, and E. F. de Lima, Controlling dissociation by trapping trajectories in highly energetic states, Physica A **449**, 101 (2016).
[90] S. M. Ikhdair, Effective Schrödinger equation with general ordering ambiguity position-dependent mass Morse potential, Mol. Phys. **110**, 1415 (2012).
[91] N. J. English and C. J. Waldron, Perspectives on external electric fields in molecular simulation: progress, prospects and challenges, PCCP **17**, 12407 (2015).
[92] B. J. Falaye, K. J. Oyewumi, S. M. Ikhdair, and M. Hamzavi, Eigensolution techniques, their applica-

tions and Fisher's information entropy of the Tietz-Wei diatomic molecular model, Phys. Scr. **89**, 115204 (2014).
[93] B. J. Falaye, S. M. Ikhdair, and M. Hamzavi, Spectroscopic study of some diatomic molecules via the proper quantization rule, J. Math. Chem. **53**, 1325 (2015).
[94] M. J. Idrissi, A. Fedoul, and S. Sayouri, Systematic approach to compute the vibrational energy levels of diatomic molecules, J. Appl. Math. Phys. **8**, 2463 (2020).
[95] P. Holmes, A nonlinear oscillator with a strange attractor, Phil. Trans. R. Soc. Lond. **292**, 419 (1979).
[96] A. H. Salas, W. Albalawi, M. Alharthi, and S. El-Tantawy, Some novel solutions to a quadratically damped pendulum oscillator: Analytical and numerical approximations, Complexity **2022**, 803798 (2022).
[97] M. Rosso and R. Ardito, A review of nonlinear mechanisms for frequency up-conversion in energy harvesting, in *Actuators*, Vol. 12 (MDPI, 2023) p. 456.
[98] J. Guckenheimer and P. Holmes, *Nonlinear oscillations, dynamical systems, and bifurcations of vector fields*, Vol. 42 (Springer Science & Business Media, 2013).
[99] S. Guruparan, B. R. D. Nayagam, S. Selvaraj, V. Ravichandran, and V. Chinnathambi, Bifurcation structures of the classical Morse oscillator under the excitation of different periodic forces, J. Adv. Chem. Sci. **2**, 188 (2015).
[100] M. W. Hirsch, C. C. Pugh, and M. Shub, Invariant manifolds, Bull. Amer. Math. Soc. **76**, 1015 (1970).
[101] Y. Yi, A generalized integral manifold theorem, J. Diff. Equ. **102**, 153 (1993).
[102] O. T. Kolebaje, O. O. Popoola, and U. E. Vincent, Occurrence of Vibrational resonance in an oscillator with an asymmetric Toda potential, Phys. D: Nonlinear Phenom. **419**, 132853 (2021).
[103] O. T. Kolebaje, U. E. Vincent, B. E. Benyeogor, and P. V. E. McClintock, Effect of a modulated acoustic field on the dynamics of a vibrating charged bubble, Ultrasonics **135**, 107110 (2023).
[104] H. E. Nusse and J. A. Yorke, Wada basin boundaries and basin cells, Physica. D: Nonlinear Phenom. **90**, 242 (1996).
[105] A. Daza, A. Wagemakers, and M. A. Sanjuán, Ascertaining when a basin is Wada: the merging method, Sci. Rep. **8**, 9954 (2018).
[106] A. Wagemakers, A. Daza, and M. A. Sanjuán, The saddle-straddle method to test for Wada basins, Commun. Nonlin. Sci. Numer. **84**, 105167 (2020).
[107] I. Selmi, M. Bejaoui, M. Farjallah, J. Dhiflaoui, and H. Berriche, Theoretical Investigation of $Cl_2$, ClO and $Cl_2O$ molecules, in *Advances in Methods and Applications of Quantum Systems in Chemistry, Physics, and Biology*, edited by I. Grabowski, K. Słowik, J. Maruani, and E. J. Brändas (Springer Nature Switzerland, Cham, 2024) pp. 199–224.
[108] J. Zhang, Z. Li, and Y. Yang, Multi-ionization of the $Cl_2$ molecule in the near-infrared femtosecond laser field, RSC Adv. **10**, 332 (2020).
[109] R. P. Wayne, Reactions involving excited states of O and $O_2$, in *Physics and Chemistry of Upper Atmosphere*, edited by B. M. McCormac (Springer Netherlands, Dordrecht, 1973) pp. 125–132.
[110] M. Bregnhøj, Introduction, in *The electronic transitions of molecular Oxygen* (Springer International Publishing, Cham, 2019) pp. 1–16.
[111] M. W. Kiehlbauch and D. B. Graves, Inductively coupled plasmas in oxygen: Modeling and experiment, J. Vac. Sci. Technol. A **21**, 660 (2003).
[112] H. Lischka, D. Nachtigallová, A. J. A. Aquino, P. G. Szalay, F. Plasser, F. B. C. Machado, and M. Barbatti, Multireference approaches for excited states of molecules, Chem. Rev. **118**, 7293 (2018).
[113] J. Vala, R. Kosloff, and J. N. Harvey, Ab initio and diatomics in molecule potentials for $I_2^-$, $I_2$, $I_3^-$, and $I_3$, J. Chem. Phys. **114**, 7413 (2001).
[114] H. Labiad, A. Faure, and I. R. Sims, Experimental evidence of quantum interferences in CO-H $_2$ rotational energy transfer at room temperature, arXiv preprint arXiv:2504.04403 (2025).
[115] P. Dral and M. Barbatti, Molecular excited states through a machine learning lens, Nat. Rev. Chem. **5**, 388 (2021).